RESEARCH: Review

Recent progresses on physics and applications of vanadium dioxide

Kai Liu [1], Sangwook Lee [2], Shan Yang [3], Olivier Delaire [3], Junqiao Wu [4],*

[1] State Key Laboratory of New Ceramics and Fine Processing, School of Materials Science and Engineering, Tsinghua University, Beijing 100084, China
[2] School of Materials Science and Engineering, Kyungpook National University, Daegu 41566, South Korea
[3] Department of Mechanical Engineering and Materials Science, Duke University, Durham, NC 27708, USA
[4] Department of Materials Science and Engineering, University of California, Berkeley, CA 94720, USA

As a strongly correlated electron material, vanadium dioxide (VO_2) has been a focus of research since its discovery in 1959, owing to its well-known metal–insulator transition coupled with a structural phase transition. Recent years have witnessed both exciting discoveries in our understanding of the physics of VO_2 and developments in new applications of VO_2-related materials. In this article, we review some of these recent progresses on the phase transition mechanism and dynamics, phase diagrams, and imperfection effects, as well as growth and applications of VO_2. Our review not only offers a summary of the properties and applications of VO_2, but also provides insights into future research of this material by highlighting some of the challenges and opportunities.

Introduction and background

Since its discovery in 1959 [1], vanadium dioxide (VO_2) has been a favorite material for research driven by both scientific curiosity and possibility of device applications, owing to the now well-known metal–insulator transition (MIT) accompanied by a structural phase transition (SPT). The MIT features a drastic change in electrical conductivity as well as resultant changes in physical properties such as optical absorption and dielectric function, while the SPT changes the material's crystal structure along with large transformation strain. Unlike most other materials exhibiting MIT or SPT, in VO_2 these two transitions are intrinsically coupled together and seem to occur concurrently, an effect that has fueled the long-lasting debate on the physics underlying the combined transition. In addition, the MIT in VO_2 occurs at a conveniently accessible temperature ($T_c \approx 340$ K), and can be driven not only via heating/cooling, but also with strain, pressure, chemical doping, as well as intense optical or electrostatic fields. These versatilities, coupled with the simple composition and relatively easy synthesis, make VO_2 a material of intense focus for materials scientists as well as device engineers seeking multiple functionalities and smart responses.

Despite decades of research on VO_2, there exist only a few review articles, which are focused specifically on band theory [2], synthesis [3], applications in electronics [4] or smart coatings [5,6], respectively. Advances in recent years yielded both exciting discoveries in our understanding of the physics of VO_2, as well as developments in new applications of VO_2-based materials. This is attributed to recent advances in scientific instrumentation, computational power, and synthesis methods that enabled new explorations. In this article, we present a comprehensive review of some of these recent progresses. Readers are cautioned that although some of the older explorations and understanding of VO_2 are introduced here as a historical context, the review is by no means comprehensive and inclusive of all existing knowledge accumulated to date.

Theory: phonons and electrons
Crystal structure
At ambient pressure, VO_2 adopts a tetragonal rutile (R) structure with space group $P4_2/mnm$ (#136) and lattice constants $a = b \approx 4.55$ Å and $c \approx 2.85$ Å [7,8] above T_c [1,9]. Below T_c, the unstrained, stoichiometric crystal structure is monoclinic

* Corresponding author.
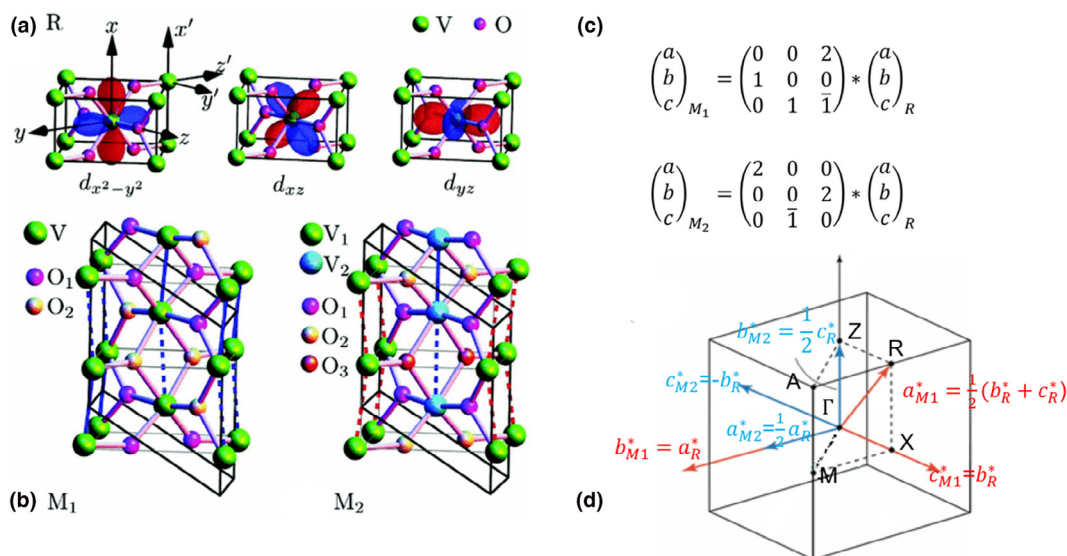 E-mail address: Wu, J. (wuj@berkeley.edu).

FIGURE 1

(a) Unit cell of rutile phase showing the 3d orbitals of t_{2g} symmetry for the center V atom, in a rotated xyz reference frame [22]. (b) Unit cell of Monoclinic M_1 and M_2 phase of VO_2 [22]. (c) Approximate lattice vector transformation matrix in real space between the monoclinic M1 phase and R phase, and M2 phase and R phase [12]. (d) Lattice vector relations in reciprocal space between the monoclinic M1, M2 phases and R phases, shown together with the Brillouin zone of the R phase [15].

(so-called M1 phase), with space group $P2_1/c$ (#14) [9] and lattice constants $a \approx 5.75$ Å, $b \approx 4.53$ Å, $c \approx 5.38$ Å, $\beta = 122.6°$ [8,10]. The M1 structure is characterized by a doubling of the unit cell volume compared to the rutile, and a dimerization pattern of V chains along the c-direction of the parent rutile phase, which includes a zig-zag pattern corresponding to dimer rotation about this direction, as shown in Fig. 1(b). The dimerization in the M1 phase results in two different V–V bond lengths: a short intra-dimer length of 2.65 Å and a longer inter-dimer length of 3.12 Å, in contrast to equally spaced V–V bonds as in the rutile phase [9,11].

Additional M2 (monoclinic, space group $C2/m$ (#12)) and T (triclinic, space group $P\bar{1}$ (#2)) phases were identified in Refs. [7,8,12–14]. These additional phases are stabilized by application of strain [8,15–17] or doping with Cr, W, or Al [7,12,14,18–20]. In the M2 phase, two different types of V chains coexist, exhibiting either a zig-zag pattern or a dimerization, but only one at a time. As illustrated in Fig. 1(b), the V chain in the middle of the unit cell exhibits dimerization, and the V chains on the edges only show zig-zag behavior. For the dimerized V chains, the V–V bond lengths are 2.538 Å and 3.259 Å for the short and long bonds, respectively, while for the zig-zag chains all V–V bonds have a single length of 2.933 Å [2]. Lattice vector transformation matrix in real space between the monoclinic M1 phase and R phase, and M2 phase and R phase, are listed in Fig. 1(c) [12], and reciprocal lattice correspondences between the monoclinic M1, M2 phases and R phases are illustrated in Fig. 1(d).

Upon transforming from R to M1, four different twins can form, which are related by 90° rotations about the rutile c-axis (in the approximate geometrical correspondence described above) [2]. It is to be noted that both the MIT transition temperature and the twinning microstructure of M1 and M2 phases depend sensitively on externally applied conditions as well as the sample history. For instance, different twin patterns appear under different conditions of strain, electrical currents applied, or the presence of defects [8,15,21].

Electronic structure

In the early work of Goodenough, the overall band structure for the metallic, R phase VO_2 was rationalized based on band theory for independent electrons [9]. According to his model, the V 3d orbital manifold splits into e_g symmetry and t_{2g} symmetry states, in response to the octahedral coordination with oxygen atoms. Because of the orthorhombic component of the local crystal-field, the t_{2g} states are further split into two d_π orbitals and one $d_\parallel$ orbital. The d_π orbitals point toward the faces of the coordination octahedron, while the $d_\parallel$ orbital points along the c_R axis, thus in the direction of the nearest V atom in the next unit cell "above" or "below" [9]. The V atom 3d orbitals are shown in Fig. 1(a). The structural zig-zag distortion leads to the upward shift of the π^* band above the Fermi energy, E_F, and drives the formation of the $d_\parallel$ bonding and antibonding states, with the dimerization of V chains along c_R increasing the bandgap [23]. In the independent electrons picture, the combination of these band reorganizations opens up the bandgap in the insulating M1 phase [9], as illustrated in Fig. 2 (from [24]).

Goodenough's early description of the electronic structure of VO_2 has provided useful chemical insight to this day, although modern theories and computer simulations of the electronic structure have introduced some important corrections. Importantly, a certain level of controversy has arisen between electronic band descriptions based on effective single-particle theories *versus* correlated electronic state descriptions rooted in the Mott–Hubbard theory.

The early chemical description presented by Goodenough [9] has remained consistent in large parts with modern electronic
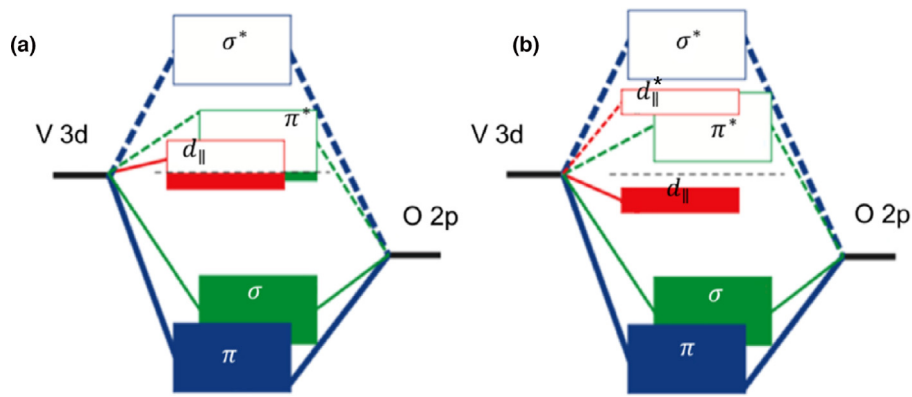
FIGURE 2

Graphic of VO$_2$ electronic band structure in the R (a) and M1 (b) phase [24].

structure simulations based on single-electron bands, for example density functional theory (DFT) simulations [2], yet with the important exception of the magnitude of the bandgap in the monoclinic phase [2]. By analyzing the conductivity and magnetic susceptibility for M1, M2, T, and R phases, Zylbersztejn and Mott concluded that a significant Hubbard U is necessary for opening the monoclinic bandgap, and that the lattice distortion alone is not sufficient for driving the MIT [25,26]. Based on their analysis of the doping effects, the electronic correlations were found to be stronger in the M1 phase than in the rutile phase, which was attributed to the screening effect on the $d_{\parallel}$, by the broad π^* band in the rutile phase [25]. However, detailed calculations of the electron quasiparticle spectral functions for both M1 and R, based on cluster dynamical mean-field theory (c-DMFT), arrived at the opposite conclusion, with the rutile metallic phase being strongly correlated while the M1 phase could be described in terms of effective quasiparticles (weaker correlation effects) [27]. In conventional DFT simulations, the effect of electronic correlations, included via a Hubbard U term (DFT + U), directly impacts predictions for the insulating phases, with predictions

of a vanishing bandgap for the insulating M1 and M2 phases (with both GGA or LDA functionals) when $U = 0$ [2,28,29]. However, DFT simulations including $U \sim 2$–4 eV [22,30] or corrections using hybrid functionals [29], which provide a more accurate treatment of exchange, are able to predict reasonable bandgaps for both M1 and M2, although the latter may still tend to be too large in comparison with the experimental values. For example, calculations with the hybrid functional of Heyd-Scuseria-Ernzerhof (HSE) predicted bandgaps of about 1.1 eV for M1, and 1.2 eV for M2 [29]. The ability of hybrid functionals to open up the bandgap within DFT would also indicate that the Hubbard interaction is not strictly necessary in explaining the MIT phase transition [29].

However, simultaneously capturing the bandgap and the correct magnetic ground state in the M1 phase has not been possible with DFT-based methods [22,31]. On the other hand, c-DMFT and first-principles quantum Monte Carlo (QMC) offer a reasonable description of the electronic structure for both the rutile and monoclinic phases [27,32,33]. Electronic densities of states for both monoclinic and rutile phase are shown in Fig. 3(a) and
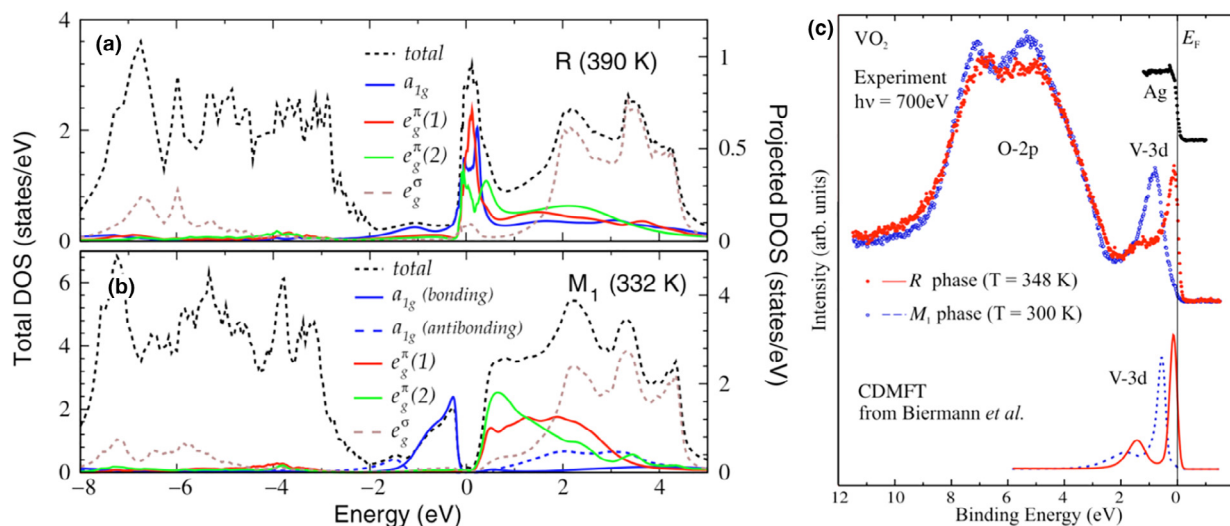

FIGURE 3

(a, b) Total and orbital-projected electron DOS for M1 and R phases, obtained from DFT + DMFT [34]. (c) X-ray photoemission spectra of rutile (red) and monoclinic (blue) phases below the Fermi level [37]. The theoretical curves in (c) are c-DMFT calculation results from [32].

(b), which are consistent in solving the difficult bandgap problem using the DFT + DMFT method. X-ray photoemission results agree reasonably well with the electron DOS calculated with DFT + DMFT [34] and previously with c-DMFT [32] in the valence band region. Still, at present, the detailed role and extent of electronic correlations in the MIT remain incompletely understood.

Numerous experimental techniques have been used to probe the electronic structure of VO_2, including optical reflectivity, X-ray photoemission, X-ray absorption spectroscopy, and electrical transport measurements [24,35–39]. Experimental measurements [35,36,40] have tended to support Goodenough's predictions of the band structure reorganization across the phase transition. However, UV reflectance and photoemission experiments found that a further opening of the bandgap besides the lattice distortion is due to the electron–electron interactions [9,35]. A recent temperature-dependent investigation of the MIT based on X-ray absorption spectroscopy on ultrathin VO_2 films proposed a three-step transition scenario on heating across the MIT [38]. A first step, several degrees below the MIT, was proposed to consist in a weakening of electron correlations. A second step was proposed to lead to the disappearance of the bandgap, and a final third step to yield the structural phase transition. By simultaneously tracking the electrical resistivity and the V dimer twisting angle probed by XAFS in fine temperature steps, Yao et al. determined a strong dependence of the resistivity on the concurrent structural distortion, but also found an intermediate monoclinic-like structure with metallic character, and concluded that the MIT could be described as cooperative Peierls and Mott transition [39].

Magnetic properties

VO_2 exhibits a large, step-like decrease (roughly an order of magnitude) in magnetic susceptibility on cooling from the R to M1 phase [40,41]. The Curie–Weiss law captures the behavior of the R phase, while in the M1 phase the magnetic susceptibility takes a smaller, constant value [41,42]. It was pointed out that the large change in magnetic susceptibility at the phase transition cannot be satisfactorily explained by the electronic structure suggested in Goodenough's model [40,41]. While *Mössbauer* experiments have shown the absence of antiferromagnetically ordered local moments in the M1 phase [41], it is thought that the R phase exhibits paramagnetic, disordered local moments [22,33,40]. In addition to the difficulty in capturing the M1 bandgap, simulating the correct magnetic state from first-principles also remains challenging for current electronic structure theories. Although DFT + U successfully opens the bandgap in the monoclinic phase, it fails to predict the correct magnetic properties of VO_2 [22]. Despite early enthusiasm [29], HSE has so far remained unable to provide physically realistic results for the magnetic properties in both metallic and insulating phases of VO_2 [22,31]. However, in a recent paper, a precise DFT calculation using the PBE0 rather than the HSE hybrid exchange functional provided correct magnetic states of both the M1 and R phases [43]. Furthermore, rigorous treatments of electronic correlations performed with a combination of Ising models and fixed-node diffusion quantum Monte Carlo were able to correctly simulate the magnetic susceptibility in both the rutile phase and monoclinic phases, offering a possible path forward for ab initio

treatments of correlation effects [33]. According to [33], net spins are present on V atoms in both phases and the R phase can be described as a moderately correlated paramagnetic metal, while in the M1 phase the spins are strongly antiferromagnetically coupled in V dimers, and this phase can be viewed as the result of a spin-Peierls transition.

Phase transition mechanism and dynamics
Peierls or Mott scenario

The mechanism of the MIT phase transition in VO_2 has been extensively investigated. Yet, despite huge efforts, a complete understanding of the driving forces and transition mechanism remains elusive. Over the years, the debate over the mechanism underlying the phase transition has intensified, primarily confronting two alternate scenarios: a lattice distortion driven (Peierls-like) or an electron correlation driven (Mott-like) transition. However, recent theoretical treatments have proposed a partial resolution to the controversy with an intermediate description in terms of "Mott-assisted Peierls" or "Peierls-Mott" pictures [27,32,44,45].

Goodenough has attributed the mechanism of the MIT to the antiferroelectric V zig-zag distortion with the assistance of V dimerization [9]. Thus, the phase transition could be interpreted as resulting from a strong interaction of electrons and phonons. Following this viewpoint, the behavior of VO_2 is often likened to a Peierls transition in a truly 1D metal chain, although the additional zig-zag distortion introduces further complexity, as recognized early on by Goodenough [9]. The electron–phonon interaction in VO_2 was also emphasized in [46–49], and proposed to lead to a softening tendency of a zone-boundary phonon mode at the reciprocal lattice point R in the metallic phase as temperature decreases. However, as revealed by recent inelastic X-ray experiments, while the entire transverse acoustic (TA) phonon branches of the rutile phase do show a softening tendency on cooling toward the MIT, the TA modes at the R point do not actually condense at the MIT, and a sharp first-order discontinuity of phonon frequencies is observed [30]. While the transition presents some aspects of a Peierls-like instability, the electron–phonon coupling does not appear sufficient to describe the entire mechanism of the MIT phase transition.

Four years after the publication of Goodenough's classic model [9], Mott and Zylbersztejn proposed that electronic correlations should be the primary effect leading to the opening the bandgap [25]. Qazilbash et al. reported an unusually broad Drude peak in the optical conductivity of the rutile phase with a width $> \sim k_B T$ [50,51], suggesting a quasiparticle lifetime shorter than the diffusive "Planckian" limit [52], characteristic of strongly interacting metals [53]. Lee et al. reported an anomalously low electronic thermal conductivity in the metallic R phase that is attributed to suppressed electronic entropy and heat transfer due to strong electron correlations in a non-quasiparticle charge transport mode [54].

From infrared spectroscopy and nano-imaging experiments, a strongly correlated intermediate metallic state was reported to occur in the MIT phase transition process, with the rutile metallic phase being a "bad metal", breaking down the "Ioffe-Regel-Mott" limit, due to strong electronic correlations observed in

the rutile phase from ellipsometry and reflectivity experiments [50,51]. A correlated metallic phase was also reported from photoexcitation pump–probe experiments, but with a crystal structure analogous to the monoclinic phase [55]. Recent resistivity studies support electron screening effect as already considered in [25], showing that the M1 phase crosses over to the metallic R phase only when the free electron density reaches a certain threshold to sufficiently screen the strong electronic correlation [56,57].

Recent theoretical treatments tend to bridge the gap between the purely Mott-like and purely Peierls-like pictures. Cluster-DMFT (c-DMFT) simulations have presented a so-called "correlation assisted Peierls transition" scenario, concluding that electronic correlations are necessary in leading the bandgap opening process [32]. Supporting this view, photoelectron and X-ray absorption spectroscopy experiments found that the spectral weight shift during the phase transition may be explained by a Peierls-like transition, based on the presence of a one-dimensional polarization of the electronic structure, itself resulting from strong electron correlation effects [37,58]. The phase transition was also theoretically considered to arise from both electronic correlations and electron–phonon interaction by Tomczak et al., and, as a result, the M1 phase was termed a "many-body Peierls" insulating state [27]. Also, based on large DFT simulation cells and complemented with c-DMFT, the MIT was characterized as a "Peierls-assisted orbital selective Mott transition" [45]. In a recent twist, a study based on first-principles quantum Monte Carlo determined the R-M1 phase transition to be a "spin Peierls-like transition" [33].

Lattice dynamics
Inelastic neutron scattering (INS) has traditionally been the most powerful method to measure the phonon dispersions and density of states (DOS). However, the difficulty to grow sufficiently large single-crystals for this method (and the tendency of large crystals to shatter at the MIT), combined with the large incoherent neutron cross-section of vanadium, have made INS measurements of phonon dispersions challenging in VO_2 [30,59]. For many years, Raman and infrared optical spectroscopy have been the main experimental techniques used to probe the evolution of phonons across the MIT [59,60] and have been complemented

by other techniques indirectly probing phonons, such as X-ray thermal diffuse scattering [49] or ultrasonic elastic constants measurements [61]. More recently, optical phonon mode frequencies can be extracted from ultrafast time-resolved reflectivity experiments [62].

Early Raman studies [59,60] identified a large reorganization of the zone-center phonon spectrum across the MIT. The comparison of Raman spectra in the high-temperature rutile phase and low temperature M1 phase revealed a pronounced damping of phonon peaks in the rutile phase [59], as seen in Fig. 4(a) and (b). The strongly broadened phonon spectrum in the rutile phase was ascribed to strong electron–phonon coupling [59]. Yet, Raman spectroscopy is limited to sampling modes at the zone-center, while it was identified in other works that wavevectors around the R-point and other extended regions of the Brillouin zone are also important [46–49]. In particular, diffuse X-ray scattering measurements identified a pronounced signal for transverse-polarized phonons with wavevectors parallel to the Γ-R direction [49].

Until recently, it has remained challenging to map the entire phonon dispersions of VO_2 across the Brillouin zone. Yet, combining inelastic X-ray measurements (IXS) on small single-crystals and INS measurements on powder samples, a detailed picture of the evolution of the lattice dynamics across the MIT was recently achieved, and supported by first-principles phonon simulations, as shown in Fig. 5(a) [30]. This study revealed that the entire phonon density of states (DOS) softens abruptly on warming across the MIT, without condensation of the TA mode at the R point, reflecting the first-order nature of the phase transition. The study also showed that low-energy TA modes involving large-amplitude, strongly anharmonic vanadium vibrations lead to a large increase in phonon entropy in the metallic phase, thermodynamically stabilizing it [30], confirming early conjectures by Paul [63] and Hearn [46].

A comparison of phonon dispersions calculated from first-principles for both M1 and rutile phases was recently reported in [54], see Fig. 5(b). The calculations for the rutile phase were performed with AIMD simulations to include anharmonic effects [54], similar to the previous calculations [30], while the phonons in the insulating M1 phase were calculated within the simpler harmonic scheme, which describes the insulating phase
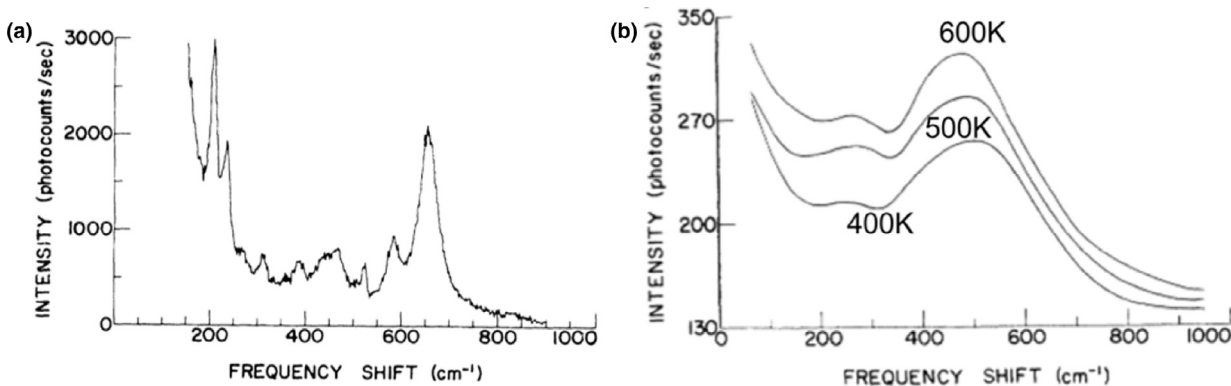

FIGURE 4

Unpolarized Raman spectra of low temperature M1 phase at 300 K (a) and of high temperature VO_2 R phase at 400 K, 500 K and 600 K (b) [59].
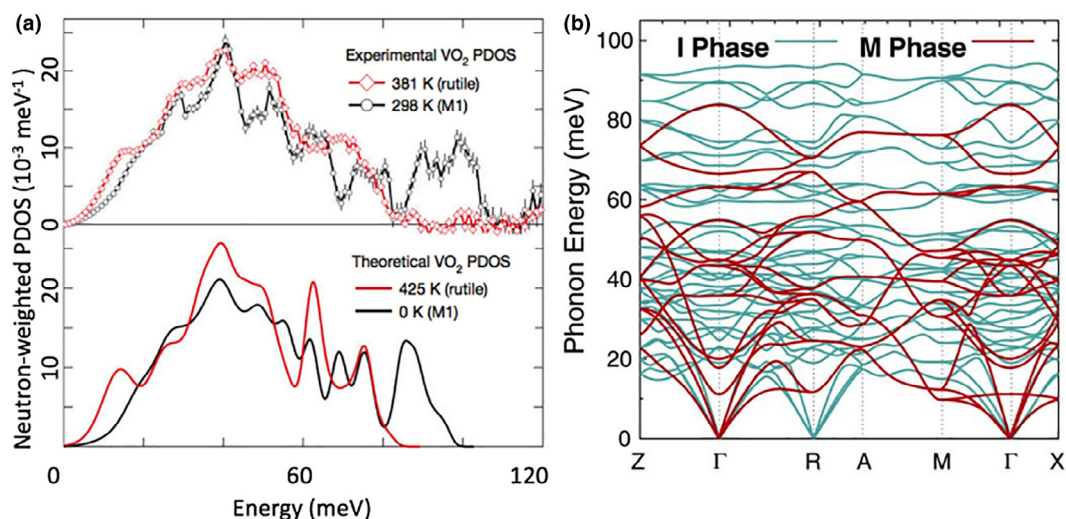
RESEARCH: Review

FIGURE 5

(a) Phonon density of states in R and M1 phases, from inelastic neutron scattering measurement and DFT based calculations [30]. (b) Calculated phonon spectrum for M1 and R phase [54].

adequately. The phonon simulations in [54] turned out to be rather unaffected by the relatively imprecise bandgap prediction for the M1 phase. These results contrast with DFT and DFT + U simulations that failed to generate stable phonon dispersions for the rutile phase, with instabilities at multiple wavevectors [64], which were contradicted with the rutile dispersion measurements from IXS [30]. This difficulty in capturing the rutile phonon dispersions with DFT is understood as a shortcoming of the harmonic approximation used by Kim et al. for the rutile phase [64], rather than a failure of DFT. On the other hand, by including anharmonic effects with AIMD simulations and a renormalized Hamiltonian, calculations of phonon dispersions for the rutile phase achieved good agreement with IXS measurements, highlighting the importance of anharmonic effects in rutile VO_2 [30].

Thermal transition and thermodynamics

The discussion of thermodynamic driving forces accounting for the phase competition in VO_2 hinges on the respective importance of electronic, magnetic, and phonon contributions to the entropy. The electronic entropy results from the finite density of states at the Fermi level in the metallic state, and thus favors the R phase over the insulating state. However, the change in electronic structure alone is not sufficient to account for the large entropy change across the MIT [25,40,46]. The vibrational entropy is generally a large quantity, a small relative change in vibrational entropy was surmised as the possible main source of the total entropy difference in the phase transition [63]. It was in particular pointed out that phonon modes sensitive to d electron bonding could be driving the increase of entropy in the rutile phase [63]. In the absence of a large magnetic entropy difference, the phonon entropy was thus proposed as the dominant contribution. However, Raman experiments [59] somewhat misleadingly concluded that the phonon softening in the rutile phase may not be the driving force for the phase transition, considering that rutile and monoclinic phase free energy decrease with increasing temperature. The role of phonon degrees of free-

dom on the MIT thermodynamics was recently clarified by detailed measurements and first-principles simulations of the phonon DOS [30]. This study showed that the phonon entropy gain from M_1 to R, arising from the large spectral softening, accounts for the larger portion of the total entropy change across the MIT [30]. Thus, the thermodynamics of the phase transition can be understood as resulting from the competition between the higher entropy of the metallic phase, provided mainly by softer phonons but partly also by the available electronic states at the Fermi level, and the lower enthalpy of the insulating M1 phase resulting from the bandgap opening [30,46,63].

Ultrafast optical studies

Ultrafast pump–probe techniques have been used extensively over the past 20 years to investigate the mechanism of the MIT in VO_2. These experiments use short laser pulses (typically a few to ~100 femtoseconds) to trigger the transition from M1 to R, while a delayed pulse of either laser light, X-rays, or electrons is used to probe the response and time evolution of the system. Current estimates of the timescale of the phase-transition range between femtoseconds and several picoseconds [55,65–67], with some discrepancy depending on the types of probe beam used. The ultrafast pump–probe approach provides a new means to control and probe the evolution of the phase transition in time, but it must be appreciated that the athermal photo-excited behavior does not necessarily reflect the equilibrium thermal behavior investigated by other techniques. In addition, as for the thermally-driven MIT, a detailed microscopic physical understanding of the ultrafast temporal evolution remains elusive. Notable unresolved questions include whether the structural phase transition occurs concomitantly with the electronic transition, and whether a metastable state exists [55,68,69], or whether the transition proceeds via a coherent soft-phonon mode. Thus, the photo-induced phase transition mechanism of VO_2 is currently a very active area of investigation.

A primary focus in ultrafast pump–probe studies is the determination of the time-scale over which the transformation occurs
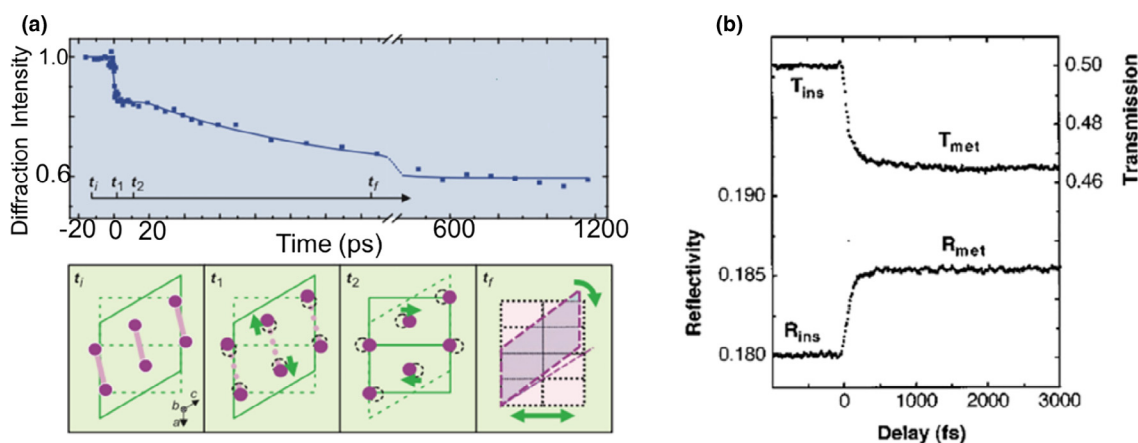
FIGURE 6

(a) The diffraction intensity change explained by stepwise structure distortion under the ultrafast electron diffraction experiment, with the corresponding multi-step structural distortion plotted below [67]. (b) Reflectivity and transmission change under ultrafast photo-excited phase transition experiment [66].

in response to the photoexcitation. As the temporal resolution in such studies improves with experimental advances, estimated upper bounds on relevant time scales have tended to decrease over the years. Early investigations identified a time delay between the photo-excitation and the completion of the MIT, as assessed optically, coined the "bottleneck" time scale [66]. This time delay was related to a phonon period, with the phonon eigenvector providing the structural distortion between the monoclinic and rutile phases [66].The phase transition time is shown in Fig. 6(b) [66]. By detecting the optical response of the VO$_2$ photo-induced transition, the time scale was determined to be below 500 fs [70]. Subsequently, a phase transition time of ∼100 fs was obtained from measurements with a pump fluence of 25 mJ/cm^2 [65]. Yet, more recently, the phase transition is reported to be "quasi-instantaneous" [71].

Importantly, the phase transition time depends on the fluence of the pump laser pulse, and the threshold fluence triggering the MIT depends on the starting temperature in M1 [65,67]. Other differences could arise depending on whether the probe is predominantly sensitive to the electronic structure or the lattice structure. Electron diffraction experiments, probing the time-evolution of the structural reorganization at the surface of a single-crystal, reported a sequence of three structural steps with a large range of characteristic time scales [67]. The first step, several hundred femtoseconds long, was associated with the V–V dimers "breaking" (equalization of inter- and intra-dimer bond lengths). A much-delayed second step, around 10 ps, was associated with straightening of the V–V zig-zag pattern (angle becoming 180°, as in rutile), while a final period lasting hundreds of picoseconds was related to strain effects as the lattice constants relax [67]. The process is illustrated in Fig. 6(a) [67]. The fastest time scale reported in this pioneering electron diffraction study is considerably longer than in all-optical pump–probe measurements with faster time resolution.

In ultrafast studies as in more traditional thermal studies, one point of view is that the phase transition exhibits Peierls character, meaning that a structural transition is necessary for, or at least directly coupled to the MIT [66]. In alternate views, the phase transition is attributed to a purely Mott scenario, based

for example on reports of a metastable "monoclinic and correlated metal phase" [68]. This question also relates to the existence of time separation between the electron reorganization and atomic rearrangement. The observation of a time delay for the structural phase transition after the electron rearrangement by high-frequency conductivity experiments also indicates that a metastable metallic state with M1-like structure could transiently exist [72]. A "monoclinic-like metallic phase" was also observed in the static equilibrium thermal driven process, detected by low energy electron diffraction experiments, but whether the two "monoclinic metallic structures" are the same remains ambiguous [73]. The existence of the metastable metallic state is also observed to be dependent on the electronic conductivity of the substrate holding the VO$_2$ specimens [74]. However, most studies do agree that the photo-induced phase transition is a non-thermal process [62,65,72,75]. Below and close to the threshold fluence, the mechanism appears to be similar to the thermally driven process. Above the threshold fluence, the phase transition takes place in roughly one hundred femtoseconds or less (with a dependence on fluence, as noted earlier), which could be explained through a reduction of the free energy barrier by changing the potential energy [65]. Similarly, pump–probe reflectivity experiments reported that the photo-excitation alters the lattice potential in the monoclinic phase, driving the lattice potential to the rutile phase potential before the structural phase transition completes [62].

Phase diagrams and imperfections
Phase diagrams with respect to lattice deformation
As a strongly correlated electron material, it is expected that the phase transition temperature and metal–insulator domain structure of VO$_2$ are coupled to its lattice, and hence are profoundly affected by strain [57,76–78]. Table 1 lists the lattice parameters of R and M1 structures, and the strain along each lattice direction in the R to M1 phase transition, together with the corresponding base vectors between the R and M1 structures. The MIT of VO$_2$ from the metallic R phase to the insulating M1 phase can be complicated at high strains or high doping which induces the M2 phase [2,17,79–82]. Free-standing, single-crystal nanomaterials,

such as nanobeams, can be subjected to uniform and continuously tunable uniaxial strain. The lack of extended structural defects in these materials allow them to withstand much higher strain (>2%) than their bulk counterpart (<0.2%) without fracturing [77], enabling *in situ* investigations of strained states that are otherwise inaccessible. Combining *in situ* microscopic imaging and micro X-ray diffraction on single domains of crystalline VO$_2$ micro/nanobeams, its phase diagram over a range of strain has been mapped out, as shown in Fig. 7(a) [83]. The free energy of M2 in undoped VO$_2$ is believed to be very close to that of M1 around T_c, making it difficult to stabilize a pure M2 phase [17].

The structural transition from M1 to R effectively shrinks the specimen along the c_R direction by $\varepsilon_0 \approx 1\%$, while the transition from M1 to M2 expands it along c_R by $\varepsilon_0 \approx 0.3\%$ [12]. Such a high strain for this inorganic material inspires applications of phase-transition based actuators (see Section Micro-actuation and micro solid engine). A triclinic phase (T) might also derive from the M1 structure, but only with a continuous change in lattice constants and angles [2,12]. Uniaxial compression (tension) along c_R direction tends to drive the M1 phase toward the R (M2) phase. The critical stress needed to trigger the transition at temperature T_c is given by the uniaxial Clapeyron equation

$$\frac{d\sigma_c}{dT_c} = \frac{\Delta H}{\varepsilon_0 \cdot T_c^0}, \qquad (1)$$

where ΔH is the latent heat of the transition.

It has been established that under white-light illumination, the insulating phase of VO$_2$ shows a brighter optical reflectivity than the metallic (R) one [76]. In-plane bending of VO$_2$ microbeams generate optically visible, self-organized triangular metal–insulator domains so as to maximally relax the strain energy [77]. Using basic beam bending theory, the stress and strain related to the evolution of these domains can be calculated, hence a phase diagram of the M1-R phase boundary was established [77]. Furthermore, atomic force microscopy (AFM) reveals a small surface corrugation which also shows up as a striped contrast in scanning electron microscopy images. Using micro-XRD analysis, the striped phase was identified to be a twinned M2 structure. Theoretically, the M2 structure has four variants with different transformation strain tensors, where every two of them can be combined to form one kind of twins. The insulating M1/M2 phases can be differentiated from the metallic R phase by their different optical contrast, and the M1 phase from the M2 phase by the surface corrugation in the latter.

The slope of the insulating (M1 or M2) – R boundary determines the latent heat of the transitions through Eq. (1). Fitting the linear part of the experimental data, one obtains a latent heat of $\Delta H = 1200 \pm 200$ Cal/mol (or 5.0 ± 0.8 kJ/mol) [83,85,86]. For the M2 phase induced by Cr doping, its resistivity has been reported to be 25% higher than the neighboring M1 phase [25]. In the beam bending experiments, the M2 phase resistivity was found to be about three times higher than that the M1 phase [83]. The fact the M2 phase is still insulating, in spite of its un-dimerized vanadium chains, has been used to argue that the MIT in VO$_2$ is electronically driven [87].

TABLE 1

Lattice parameters of R and M1 phases.

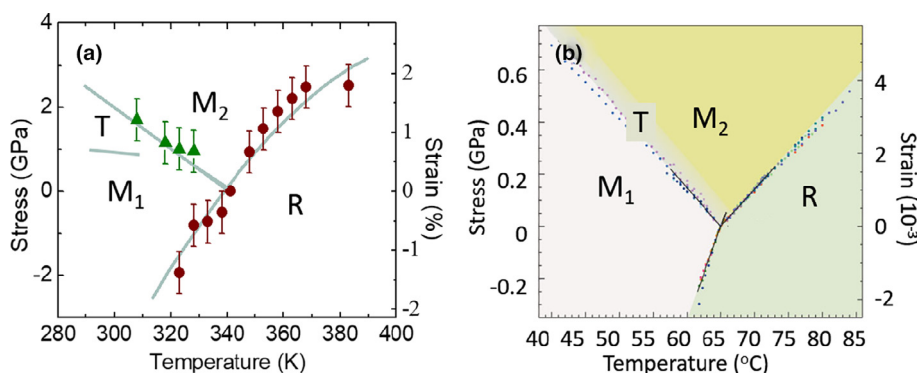| Lattice constants [2,7,8,10] [Å]		Angle [2,7,8,10] [°]		Corresponding vectors [83,84]	Length change [12,77,84] (i.e. strain)	Volume change [12,77,84]
R	**M1**	**R**	**M1**	**R ↔ M1**	**R → M1**	**R → M1**
$a_R = 4.55$	$a_{M1} = 5.75$	$\alpha = 90$	$\alpha = 90$	$\vec{a}_R \leftrightarrow \vec{b}_{M1}$	−0.6% (a_R direction)	+0.3%
$b_R = 4.55$	$b_{M1} = 4.53$	$\beta = 90$	$\beta = 122.6$	$\vec{b}_R \leftrightarrow \vec{c}_{M1} + 1/2\vec{a}_{M1}$	−0.1% (b_R direction)	
$c_R = 2.85$	$c_{M1} = 5.38$	$\gamma = 90$	$\gamma = 90$	$\vec{c}_R \leftrightarrow \vec{a}_{M1}$	+1% (c_R direction)	

FIGURE 7

(a) Uniaxial (along c_R-direction) stress – temperature phase diagram of VO$_2$ [83] mapped by imaging domain structure of bent VO$_2$ nanobeams [77]. The small stripe of T phase between the M1 and M2 regions was obtained from Raman spectroscopy of bent VO$_2$ nanobeams [88]. (b) A refined measurement of the phase diagram at small strains identifies the triple point of M1, M2 and R phases converging to zero strain [16]. Note that most of the samples measured have sizes larger than hundreds of nm, so no size effect is expected in the phase diagram.

By studying individual single-crystal VO$_2$ nanobeams in a purpose-built nanomechanical strain apparatus, Park et al. inves-
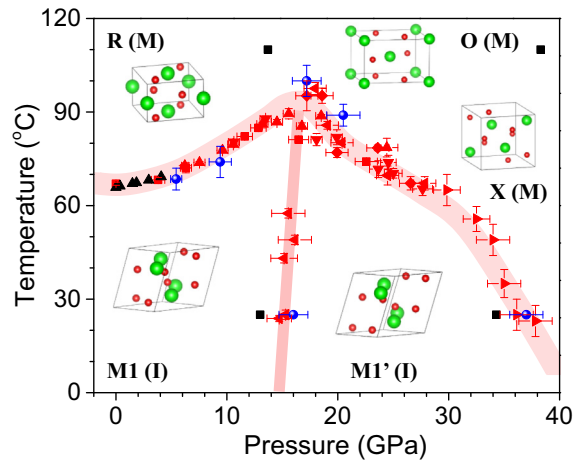

FIGURE 8

Hydrostatic pressure – temperature phase diagram of VO$_2$ [91]. I and M in parenthesis represent insulating and metallic phases, respectively. Insets are the simulated atomic structures of each phases of VO$_2$ (V: green atoms, O: red atoms). The red and blue data points on the phase boundaries are obtained from Raman and electrical measurements, respectively, and different shapes of symbols represent different samples. The black square data points are determined by XRD extracted from Ref. [89]. The black triangle data points are from Ref. [86].

tigated the phase diagram near the M1-M2-R triple point with unprecedented control and precision [16]. It was revealed that the triple point of the metallic phase and the two insulating phases is precisely at the zero-strain MIT temperature (Fig. 7(b)), i.e., the free energies of all the three phases are degenerate at the triple point in unstrained, undoped VO$_2$. These facts are not straightforward viewed from any of the current theories of the transition, and shed light onto the MIT of VO$_2$ for a full understanding of the transition mechanism.

In addition to temperature and uniaxial compression, hydrostatic pressure can also drive the M1-R transition. The application of hydrostatic pressure is a clean and powerful way to tune the lattice and electronic degrees of freedom. Hydrostatic pressure applied via a diamond anvil cell (DAC) has been able to drive the M1 phase to another isostructural, more conductive M1′ phase, and finally a new metallic X (monoclinic) phase at room temperature, as well as to drive the metallic R phase to new metallic O (orthorhombic) and X phases at 383 K [89]. A schematic pressure–temperature phase diagram had been proposed for VO$_2$ [90], lacking details especially at high pressures. In a recent work, Chen et al. established a clear hydrostatic pressure–temperature (P–T) phase diagram for VO$_2$, quantitatively delineating the phase boundaries between the M1, M1′, R, O, and X phases, and providing comparisons to first principles calculations (Fig. 8) [91]. The established phase diagram may serve as an instructive benchmark for ultimate elucidation of the phase transition physics of VO$_2$, as well as its potential applications.
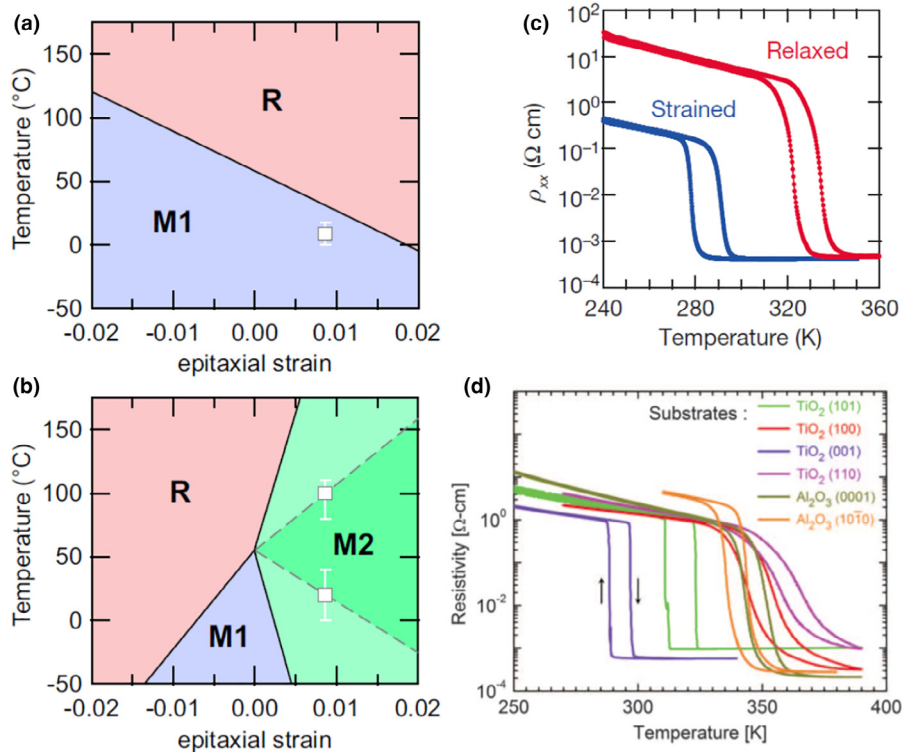

FIGURE 9

(a) Proposed phase diagram and experimental data of biaxially strained (001)$_R$ VO$_2$ films where the strain is equal in a$_R$ and b$_R$ directions [92]. (b) The same for anisotropically strained (100)$_R$ VO$_2$ films plotted as a function of the b$_R$ strain where the c$_R$ strain is fixed to be 4.35 times higher. (c) Experimentally measured MIT for VO$_2$ films pseudomorphically strained (when thickness is 10 nm) or relaxed (when thickness is 70 nm) grown on (001) TiO$_2$ substrates [93]. (d) Experimentally measured MIT characteristics of VO$_2$ films grown with different thicknesses on different substrates [95].

The phase diagrams above were all obtained from free-standing microcrystals. For device applications, on the other hand, thin films are more suitable and hence attract more attention. Thin films of VO_2 can be grown epitaxially on a range of substrates such as TiO_2 and Al_2O_3 [92–94]. Different cuts of these substrates dictate the crystal orientation of the VO_2 films, while the films can be pseudomorphically strained or strain-relaxed depending on the thickness of the epitaxial films. Shown in Fig. 9(a) and (b) are the proposed phase diagram of VO_2 films strained by misfit with (001) or (100) TiO_2 substrate, respectively [92], while Fig. 9(c) shows the MIT curve of VO_2 films grown on (001) TiO_2 substrates under strained (when film thickness is 10 nm) or relaxed (when thickness is 70 nm) condition [93]. It can be seen that the trend in Fig. 9(a) agrees with that in (c) as both are equal-biaxial strain in the a_R-b_R plane, and both are thermodynamically consistent with the phase diagram in Fig. 7(a) for uniaxial stress along the c_R axis. Fig. 9(d) shows resistivity-temperature curves of VO_2 films grown with different thicknesses on a wide range of substrates [95]. It is clear that the MIT characteristics of VO_2 films can be engineered by selection of substrate and the film thickness. The giant change in resistance also suggests applications for transistors and electrostatically driven switches (see Section Transistor and electrostatically driven switch).

Effects of non-stoichiometry, defects, and doping on the MIT

Oxygen non-stoichiometry is known to critically affect the physical properties of transition metal oxides, even for small (~a few%) deviations of the stoichiometric compositions. The oxygen non-stoichiometry effect is especially significant in VO_2. The insulating phase of VO_2 becomes more conductive with oxygen deficiency, as oxygen vacancies are typically electron donors. More importantly, the MIT temperature (T_c) of VO_2 is sensitive to the stoichiometry. As shown in Fig. 10(a), T_c of VO_2 typically decreases with oxygen deficiency [96] and

increases (although slower) with oxygen enrichment [97]. This is consistent with the recent report that hydrogen diffusion in VO_2 tend to reduce VO_2 and stabilize the metallic phase [98]. It is experimentally challenging to determine the exact amount of oxygen deficiency in oxides. Recently, a pseudo phase diagram of VO_2 has been sketched (Fig. 10(b)) for oxygen deficiency by thermally annealing VO_2 microcrystals in reducing conditions [99]. It has also been reported that by annealing in low oxygen pressure conditions, VO_2 films can be reduced from V^{4+} toward V^{3+} state and as a result the sample becomes metallic down to cryogenic temperatures [100]. It is noted that due to the multi-valence of vanadium, the phase diagram of V and O is extremely complicated. Tens of stable vanadium oxides exist at room temperature with completely different crystal structures and physical properties [101–103]. Deviating from the VO_2 stoichiometry, two special classes of oxides (VO_x) are notable, called Magneli phases ($V_nO_{2n-1} = VO_{2-1/n}$) and Wadsley phases ($V_nO_{2n+1} = VO_{2+1/n}$), respectively [104]. The Magneli phases consist of corundum- and rutile-like layers and consequently show structural similarity to both the dioxide and the sesquioxide [105]. It is interesting to see that most of the Magneli phases have a MIT at certain temperature, as shown in Fig. 10(c) [106], although the physical mechanisms of the phase transitions vary widely for the Magneli oxides [107]. It can be seen in Fig. 10(c) that these T_c do not seem to show a simple trend with the vanadium/oxygen ratio, although some semi-empirical efforts have been made in attempt to find a systematic behavior [108]. The Wadsley phases, on the other hand, exhibit no MIT except for V_6O_{13} [109]. Many of these Wadsley phases are layered structures and find applications as cathode materials for rechargeable batteries.

Vacancy and interstitial defects, called native point defects, are major concerns for semiconductor materials. In semiconductors, they can donate, trap, or scatter free charge carriers, as well as introduce local strains and mass disorder to scatter phonons,
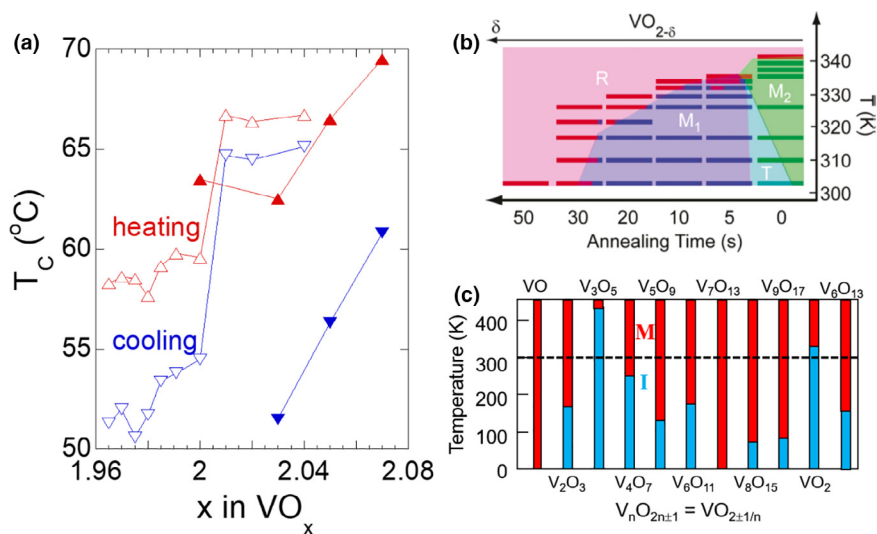

FIGURE 10

(a) MIT temperature of VO_2 as a function of oxygen non-stoichiometry [96]. (b) Raman-determined phase diagram of non-stoichiometric VO_2 obtained by thermal annealing under reducing conditions [99]. (c) MIT temperatures of the Magneli phase vanadium oxides V_nO_{2n-1} [106]. The only Wadsley (V_nO_{2n+1}) phase that has a MIT is also shown (V_6O_{13}).

hence strongly affecting the materials electrical and thermal conductivities. Although VO_2 is not considered a traditional semiconductor, the effects of native point defects in its insulating phase can be discussed in the framework of an unintentionally n-type semiconductor, as typically free electrons with a density of 10^{18}–10^{19} cm^{-3} exist in the insulating phase arising from the native defects. It is found that the insulating phase conductivity increases when more native defects are introduced, attributed to more free electrons donated to the conduction band by the native defects. These native defects can be introduced with high-energy ion irradiation. The bombardment of these ions at high energies damages the lattice, displacing V or O atoms from the original lattice sites and creating V and O vacancies and interstitials. The density of these defects depends on the irradiation dose. Typically the specimen needs to be thinner than the projected range (average implantation depth) of the impinging ions such that the ions go through the specimen completely without doping it, leaving behind only native defects uniformly distributed in the specimen. The metallic phase, on the other hand, typically becomes a poorer conductor after introduction of the defects, because the defects reduces the mobility of free electrons [110]. These native defects also strongly affect the MIT characteristics. In single-crystal VO_2 nanobeams and nanoparticles, it is found that the irradiation narrows the MIT hysteresis, as shown in Fig. 11(a) [21,111]. This is explained by the defects acting as additional nucleation sites for the first-order phase transition, facilitating the MIT and suppressing super-cooling and super-heating effects in the MIT [21]. For VO_2 thin films clamped on substrates (Fig. 11(b)), on the other hand, the hysteresis loop size is not significantly affected, while the MIT quality (i.e., the resistivity ratio and the sharpness of the resistivity curve) becomes worse upon irradiations, as shown in the samples irradiated by ^{238}U swift heavy ions [112] or O$^+$ ions [113].

Extrinsic doping and alloying have been used as a powerful means to tune the phases and MIT temperature of VO_2 [12–14,20,114–127]. In this case, the vanadium atoms (cation) are substituted with another metal element. As shown in Fig. 12(a), the MIT temperature is sensitive to such substitution. Typically, dopants with valence higher than that of vana-

dium (4+) tend to reduce the MIT temperature [128,129], with W being the most effective one, reducing T_c at up to ~27 K/at. % of doping [130–133]. The lowest T_c demonstrated is ~−50 °C for W doping of ~7.5 at.% [132] or 2.4 at.% [19]. In contrast, dopants with valence lower than that of vanadium tend to enhance the MIT temperature [128,134], with Ga being the most effective one, increasing T_c at ~8 K/at.% but only for Ga fractions up to ~1% [123]. The highest T_c is demonstrated at ~100 °C for $Cr_{0.2}V_{0.8}O_2$ [128], or at ~93.6 °C for $Ge_{0.059}V_{0.941}$-O_2 [135], although the MIT becomes much less sharp than that of undoped VO_2. The readers are cautioned that, the valence states of these dopants are not directly and experimentally confirmed, as many dopants (such as Fe, Cr and Mn) are themselves multivalent [136]. In addition, the dT_c/dx values vary widely depending on the quality, preparation methods, post-growth processing, and forms (i.e., thin film vs. bulk) of the materials. Moreover, these dependences are limited to their maximum dopant fractions, beyond which the MIT would disappear, or the materials enter a more complicated phase diagram involving phases other than the M1 and R structures. Although the doping mechanism has not been fully established, it is generally believed that the additional free electrons donated by substitutional dopants with valence higher than the 4+ of vanadium (hence electron donors) tend to screen the electron–electron correlation in the insulating state, hence lowering T_c; on the other hand, dopants with valence lower than 4+ are electron acceptors and tend to weaken the electrostatic screening from the background free electrons, and increase T_c. The internal pressure induced by the dopant atomic size mismatched with that of vanadium also plays an important role in the T_c dependence. Fig. 12(b) shows schematically the phase diagram of VO_2 against doping [137], in comparison to oxygen non-stoichiometry and c_R-axis stress. It can be seen that these three driving forces could be qualitatively mapped onto each other, leading to similar consequence on the phases of VO_2, although the former two are chemical while the last one is physical means. These connections further testify a deep relationship between the electronic and lattice degrees of freedom in VO_2 [32,45]. Doping with lanthanide elements (i.e., Tb, Eu and La) [138,139] and
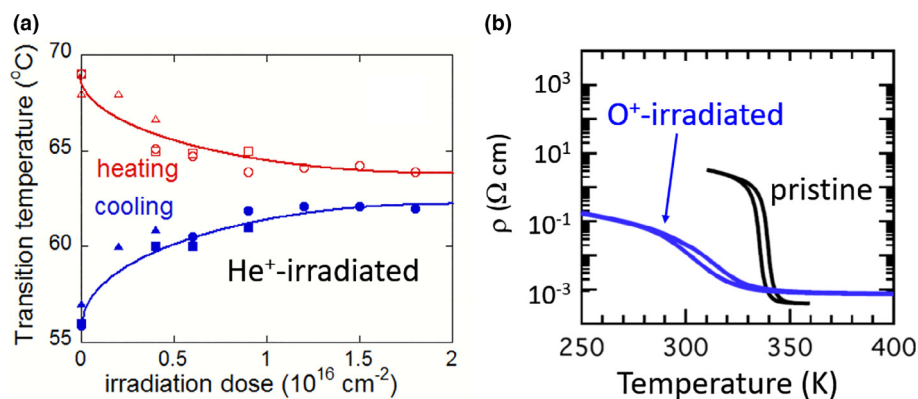

FIGURE 11

(a) Heating and cooling MIT temperatures as a function of the dose of 3 MeV He$^+$ irradiation on single-crystal, strain-free VO_2 nanobeams, showing closing of the hysteresis loop at high vacancy and interstitial defect densities [21]. (b) Resistivity – temperature characteristics of a VO_2 thin film after high (2 × 10^{15} cm^{-2}) dose irradiation of 110 keV O$^+$ ions [113]. The MIT quality and the MIT temperature are both reduced.
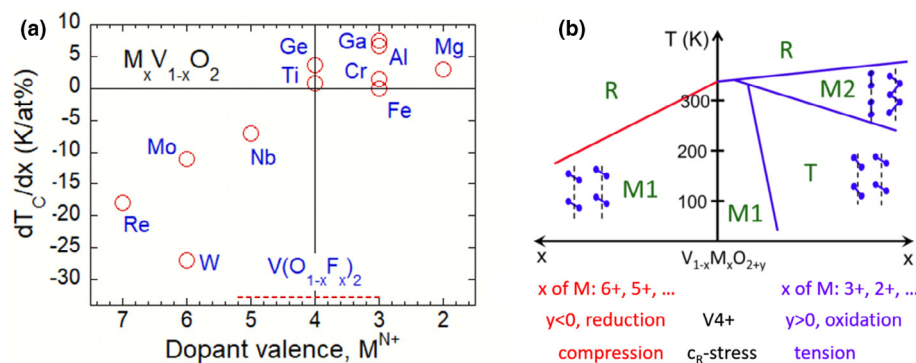
FIGURE 12

(a) Changing rate (dT_C/dx) of the MIT temperature with dopant atomic fraction (x) for cation substitutional doped VO$_2$. The data of $dT_C/dx = -32$ K/at.% for anion F-doped VO$_2$ is also indicated with a dashed line [116]. Note that the real valence state of the dopant was not directly confirmed as many of the dopants are multi-valent (e.g., Fe, Cr). (b) A schematic phase diagram of VO$_2$ for doping, non-stoichiometry, and uniaxial stress [137].

quaternary alloys involving two dopants (i.e., co-doped with Mg and W) have also been demonstrated [127].

Controlled growth of VO$_2$ thin films and nanowires

Thin films growth and characterization

Crystals of VO$_2$ can be synthesized by several well-established bulk growth processes (e.g., hydrothermal process), as adopted in Morin's pioneer work [1]. From the viewpoint of applications, however, VO$_2$ materials in the forms of thin films or nanowires are more desired for both macro- and micro-scale devices, as these forms of VO$_2$ are more compatible to materials processing and microfabrication. In this section, we focus our review on recent advances in controlled growth of VO$_2$ thin films and nanowires.

Precise phase control is not easy in growth of VO$_2$ films due to the complex phase diagram of VO$_x$ with different stoichiometries. The oxygen to vanadium ratio has been shown to greatly influence the phase transition of thin films even for small deviations, as discussed in detail in Section Effects of non-stoichiometry, defects and doping on the MIT. In the last several decades, researchers have devoted extensive efforts to grow thin films with the pure VO$_2$ phase. Major methods include chemical vapor deposition (CVD) [140–144], reactive evaporation [3], sol–gel deposition [5,145–147], sputtering [101,148–150], and pulsed laser deposition (PLD) [110,151–153].

The key to synthesize pure VO$_2$ thin films is to precisely control the stoichiometry to avoid the formation of oxygen defects and other stoichiometric ($x \neq 2$) phases by regulating the growth conditions. In CVD syntheses, for example, organic vanadium (III), (IV), or (V) compounds are employed as the vanadium precursor, and VO$_2$ films could be formed on the substrate in oxidizing, neutral, or reducing environment which depends on the precursors used [140–144]. Such a delicate control of growth conditions is also required in solution-based synthesis of VO$_2$ thin films (e.g. sol–gel deposition) for large-scale applications.

Sputtering and PLD are widely used to prepare high-quality VO$_2$ thin films. In either method, the oxygen partial pressure is the key factor to affect the MIT of the product. Using radio frequency (rf) sputtering of a vanadium target, VO$_2$ thin films were prepared under an argon–oxygen atmosphere with the oxygen partial pressure ranging from 0.5 to 2.5 mtorr [101,148]. In the study, the MIT temperature and the ratio of resistivity change across the MIT were indeed found to critically depend on the oxygen partial pressure.

In VO$_2$ thin films, the grain size is also a factor to affect their MIT behavior [149,150]. The changes of both optical and electrical properties across the MIT relate to the microstructures of the films as well as the roughness of the film surface [149]. VO$_2$ thin films with different grain sizes were grown by controlling the thickness of the films in rf-magnetron sputtering (Fig. 13(a–c)). With increase in the grain size of the film, the ratio of resistivity increases while the temperature range of the MIT decreases (Fig. 13(d)).

In recent years, VO$_2$ thin films comprising nanopores [154] and core–shell composites [155] were also prepared for specific applications. It is noted that with delicate control of the growth condition in various methods, doped VO$_2$ thin films were also prepared with modified MIT temperatures, many of which have been reviewed in Section Effects of non-stoichiometry, defects and doping on the MIT. The epitaxial strain imposed by lattice mismatch with the substrate also has a profound influence on the MIT of VO$_2$, as reviewed in Fig. 9.

VO$_2$ nanowires synthesis and characterization

As noted in Section Phase diagrams with respect to lattice deformation, VO$_2$ in the form of single-crystal nanowires or nanobeams generally shows a more abrupt, intrinsic MIT than epitaxial thin films. Other types of VO$_2$ nanostructures are sometimes also desired over thin films for various reasons such as ease of processing and low cost of preparation. In general, high-quality VO$_2$ nanostructures have been synthesized via solution-based chemical processes including sol–gel [156] and hydrothermal methods [157–160], or via physical vapor transport methods (VTM) [161–167]. Hydrothermal methods are convenient to synthesize sub-micrometer particles with a wide range of sizes, shapes, compositions, and structures in large quantity. They have been popularly used to synthesize VO$_2$ nano- and micro-crystals, since Morin reported preparation of 0.1-mm scale VO$_2$ crystals via the hydrothermal method in 1959 [1]. Recently,
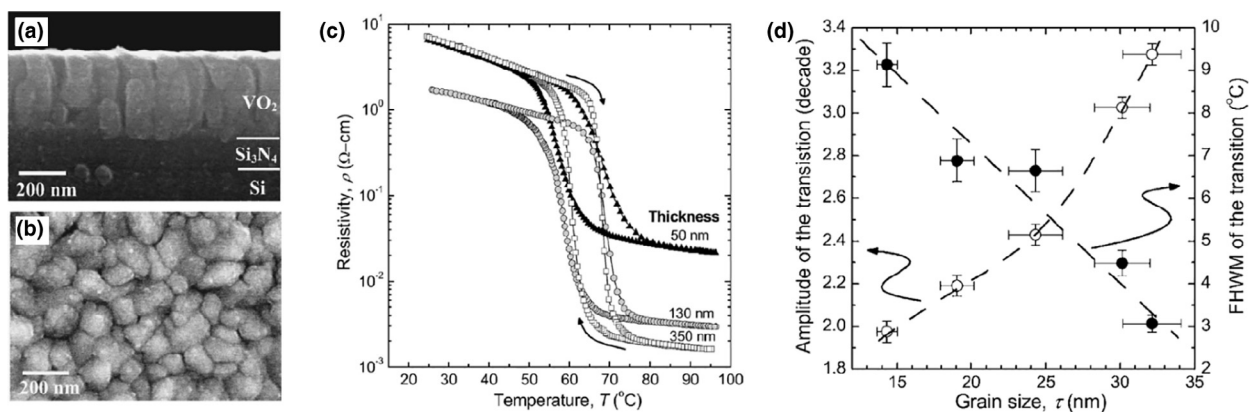
FIGURE 13

(a) Side view and (b) top view of a 350-nm-thick VO_2 film deposited by magnetron sputtering [150]. (c) MIT of VO_2 thin films with different thicknesses. (d) Dependence of amplitude and FHWM of transition temperature of the MIT of VO_2 thin films on grain size [150].
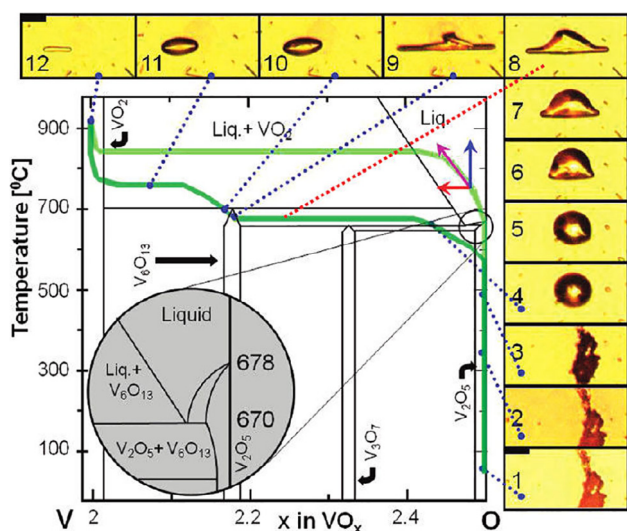

FIGURE 14

A temperature-composition phase diagram of VO_x ($\sim2 < x < 2.5$) with optical micro-images (1–12), showing chemical and morphological evolution of V_2O_5 micro-particles upon heating with a low heating rate, in which case evolution of VO_x follows the dark green line. In the case of high heating rate (500 °C/min), the evolution follows the light green line. The inset is enlarged diagram of the eutectic point [165].

several new hydrothermal methods have been also developed to synthesize VO_2 single crystalline nanowires [157–159].

VTM is one of the most widely employed methods for synthesizing VO_2 nanowires to investigate and exploit the intrinsic phase transition characteristics of VO_2. Historically, VO_2 nanowires were believed to grow from a preferential facet of VO_2 nuclei through condensation of evaporated VO_2 precursors [161,162]. Later, it was revealed that the evaporated and condensed precursor are a trace of V_2O_5, and that preformed VO_2 seeds are not needed for the growth [163,164]. Using an in-situ optical and photoelectron emission microscopy, Strelcov directly observed that V_2O_5 evaporates at low temperatures ($<\sim700$ °C), and forms V_2O_5 droplets on the substrate, which transform to VO_2 nanowires via reductive reactions in inert atmospheres (vacuum or Ar) at higher temperatures ($>\sim800$ °C) [165]. When the heating rate is high (ca. 500 °C/min), VO_2 nanowires crystallize directly from the molten V_2O_5 droplets. In contrast, when the heating rate is very low, the product undergoes multiple phase transformation through compositionally different intermediate phases, such as V_2O_5, V_6O_{13}, and VO_2, as shown in Fig. 14 [102,165,168]. During the transformation, the VO_2 grows in its R phase along the c_R axis to minimize exposure of facets with the highest surface energy [165]. VTM-grown VO_2 nanowires usually have the shape of a beam (i.e. rectangular cross section) exposing the {011} facets [169,170], as shown in Fig. 15(a).
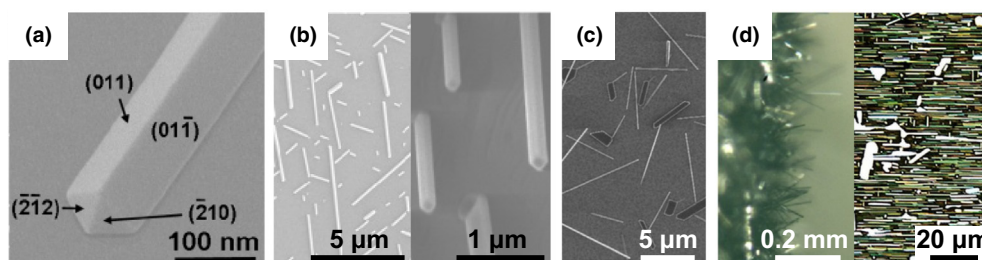

FIGURE 15

(a) SEM image showing a VO_2 nanowire with Miller indices of its facets at both the tip and the side [170]; (b–d) VO_2 nanowires grown via VTM on various substrates: (b) SEM images of nanowires grown on a c-cut (left panel) and a r-cut (right panel) sapphire substrates [170], (c) SEM image of laterally grown, randomly oriented nanowires on silicon (110) [171], (d) optical images of free-standing nanowires grown on a rough quartz substrate (left panel) [167] and laterally grown nanowires on an a-plane quartz surface (right panel) [172].
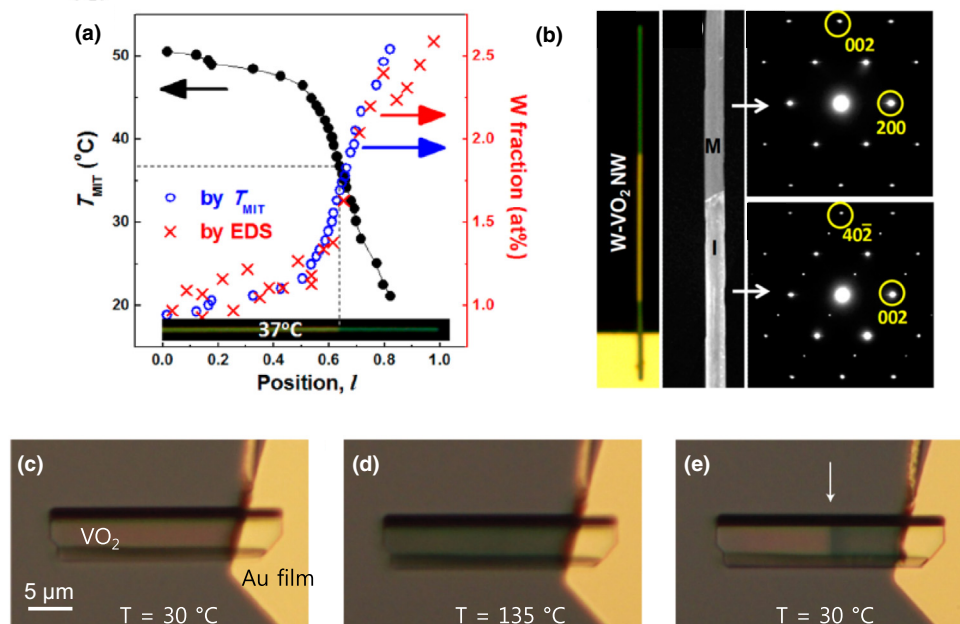
FIGURE 16

(a) Local MIT temperature (left axis) and tungsten fraction (right axis) of an axially graded-doped $W_xV_{1-x}O_2$ nanowire. The horizontal axis is positioned along the graded-doped nanowire from the center (l = 0) to the tip (l = 1). The inset shows optical image of the analyzed nanowire at 37 °C as an example. (b) Optical (left panel) and TEM (middle panel) images with the SAED patterns (right panels) corresponding to the metallic (R, upper-right panel) and insulating (M1, lower right panel) domains [166]. (c–e) Optical images showing hydrogenation of VO₂: a VO₂ micro-crystal in H₂ atmosphere at (c) 30 °C, (d) 135 °C, and (e) at 30 °C (after cooled down from 135 °C) [98]. The right bright region is gold film deposited to cover the end of the VO₂ crystal. A domain boundary, indicated by the arrow in (e), implies that the hydrogen doping fraction varies axially along this crystal.

Many types of substrates have been tested for growing VO₂ nanowires via VTM, to control the length, width, and density of the nanowires, because interactions with the substrate and capillary forces can vary with different substrates and different crystallographic directions of substrate. VO₂ nanowires with lengths up to 5 mm [167] have been grown from the condensed liquid droplet. As shown in Fig. 15(b–d), substrate-bound or free-standing VO₂ nanowires with a wide range of morphologies can be grown with or without epitaxy on these substrates.

Doped-VO₂ nanowires can be synthesized using the VTM by simply mixing the desired dopant (W, Al, and Cr) into the precursor source at controlled weight ratios [54,132,137,166]. Recently, axially tungsten (W) graded-doped VO₂ nanowires were also reported, as shown in Fig. 16(a, b). The mechanism of the graded doping of W is not clear, but it was suggested that the W dopant atoms may diffuse into VO₂ nanowires along their c_R axis under the growth condition but after the VO₂ nanowires are formed [166]. Similarly, there is another interesting report that VO₂ nanowires can be doped with hydrogen by annealing at temperatures up to 135 °C in hydrogen atmosphere when the nanowires are in direct contact with some catalytic metals (Au, Pd, Cu, and Ni) Fig. 16(c–e), in which case the hydrogen is observed to diffuse rapidly along the c_R axis [98].

Applications of VO₂

Infrared detection and bolometer

One of the promising applications using the MIT of VO₂ is for infrared detection by temperature sensing, known as bolometer.

Micro-bolometer is a device sensing the intensity of incident infrared light by monitoring the resistance change of the detecting layer in response to heating when the material absorbs the incident infrared light. For a high-performance micro-bolometer, it is required that the detecting material have a high temperature coefficient of resistance (TCR) for high sensitivity, and a low resistivity (ρ) to minimize thermal noise and Joule heating. High TCR and low ρ are competing requirements for conventional materials. VO_x-based materials have been used for micro-bolometers, because they can exhibit relatively high TCR (2–3%/K) and low ρ (0.05–0.1 Ω·cm) [173,174].

VO₂ is a strong absorber in the mid-far infrared spectrum [110,175]. Moreover, VO₂ has a high TCR in the vicinity of the MIT, and a low resistivity toward and in the metallic phase. However, VO₂ has limitations as a detecting material for micro-bolometers due to: (i) its abrupt, first-order phase transition within a narrow window of temperature which could obstruct linear, continuous sensing of temperature, (ii) its hysteresis in resistance between heating and cooling processes, and (iii) its high resistivity ∼1 Ω·cm in the insulating phase. Significant efforts have been devoted in utilizing VO₂ as detecting bolometer material by broadening the temperature window of the MIT with employing polycrystalline thin films, reducing the hysteresis by using small temperature differences, and lowering the resistivity by doping [173,176]. Especially, W-doped VO₂ thin films were reported to have a high TCR over 10%/K with a continuous sensitivity across the MIT, and a resistivity of the insulating phase lowered by an order of magnitude. Recently, it is reported that graded-doped $W_xV_{1-x}O_2$ nanowires are promising as a new,
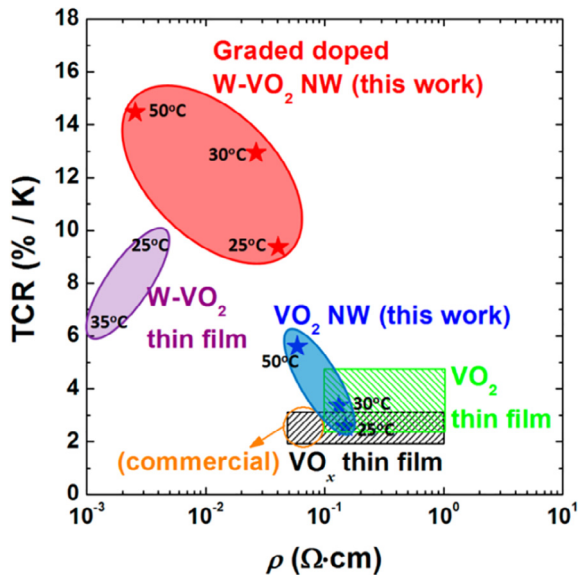
FIGURE 17

Temperature coefficient of resistivity (TCR) and resistivity (ρ) of graded-doped $W_xV_{1-x}O_2$ nanowires compared with various sensing materials, including VO_x thin films, VO_2 thin films, W-doped VO_2 thin films, and different types of VO_2 nanowires [166].

superior bolometer material. The graded-doped $W_xV_{1-x}O_2$ nano-wires exhibit a high TCR > ∼10%/K and a low ρ ranging from 0.001 to 0.1 Ω·cm, resulting from the continuously progressive decrease in resistance across the gradual MIT with increasing temperature, in contrast to the abrupt MIT of un-doped nano-wires [166], as shown in Fig. 17 [166]. For practical applications in infrared imaging, however, more engineering issues need to be solved such as to align the nanowires on the substrate to form arrays as micro-bolometer sensing components.

Thermochromics

Thermochromic materials are needed in "smart windows" that can intelligently control the intensity of transmitted light in response to environmental temperature. The thermochromic function refers to the change in light absorption coefficient of the materials in response to external thermal, electro-thermal, or photo-thermal stimulus. As VO_2 transforms from the M1 to R phase, its bandgap vanishes, leading to drastic changes in optical constants and light absorption. This characteristic makes VO_2 a promising material for smart window application. Fig. 18(a) shows the light absorption spectrum of a VO_2 film at different temperatures [110]. The light absorption of the metallic phase is much stronger than that of the insulating phase over a wide
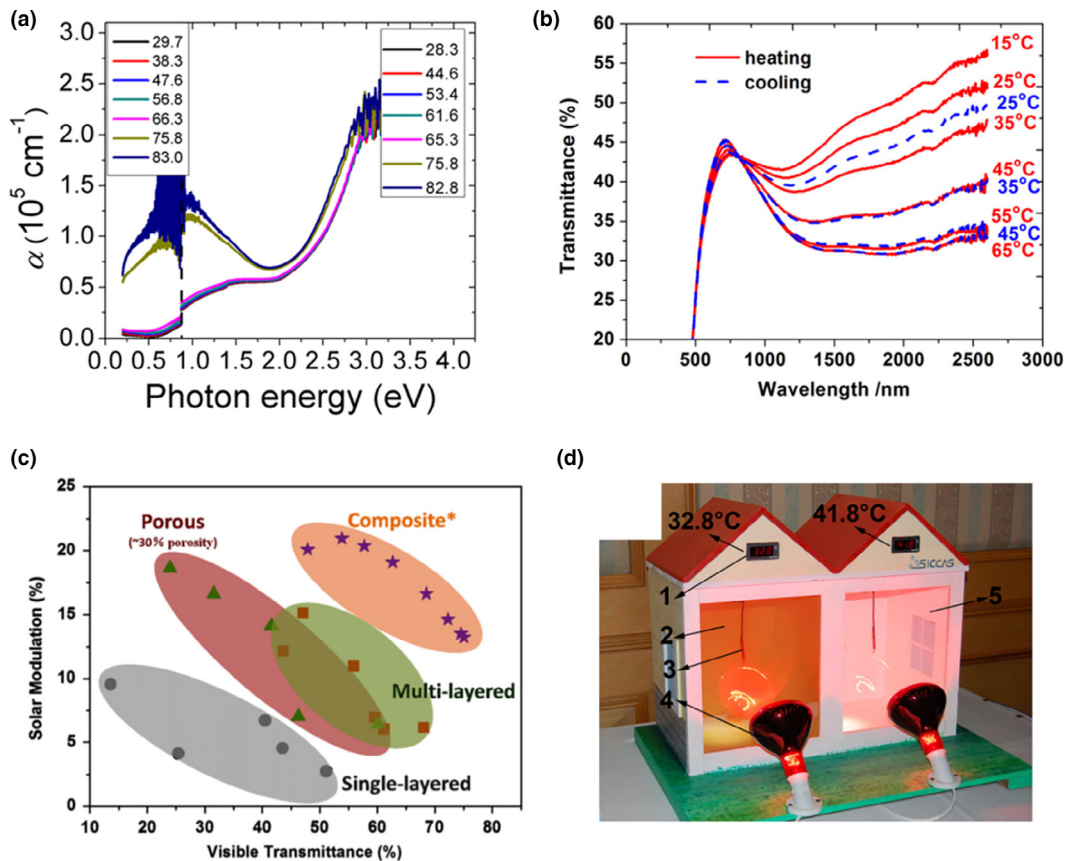

FIGURE 18

(a) Absorption coefficient of a VO_2 thin film (deposited on sapphire by PLD) at different temperatures (in units of °C) [110]. (b) Dependence of transmittance spectra on temperature for a W-doped VO_2 film [5]. (c) Thermochromic performance of different structures based on VO_2 thin films [5]. (d) A model house with a window coated by W-doped VO_2 film (left) *versus* with a blank glass window (right). 1, Temperature monitor; 2, glass coated by W-doped VO_2; 3, temperature sensor; 4, infrared lamp; and 5, blank glass [5].

range of spectrum, including the visible light (1.6–3.2 eV). In the infrared range (particularly < 0.7 eV), VO_2 is almost transparent in the insulating phase but translucent in the metallic phase [110].

However, there are also challenges for using VO_2 thin films in this application [6]. First, the MIT temperature needs to be lowered, preferably to around room temperature. This is to implement the thermochromics of VO_2 under low levels of triggering conditions, for example, to regulate the house temperature near a set room temperature, or under illumination of sun light or application of a small voltage. A large number of elements can substitutionally dope VO_2 to decrease its T_c, as discussed in Section Effects of non-stoichiometry, defects and doping on the MIT. Fig. 18(b) shows that the transmittance of a W-doped VO_2 thin film in the infrared spectrum decreases gradually with increasing temperature (from 15 to 65 °C). Substitutional doping was also found to be an effective way to improve the transparency in the visible spectral range, and to maximally eliminate the yellow color of VO_2 films that is undesired to human vision [129,177,178].

Second, for the practical applications of smart coatings, both the visible light transmittance and the solar modulation capability of the VO_2 thin films need to be improved. Growth of high-quality VO_2 thin films on buffer layers with structural similarity, including ZnO, SnO_2, TiO_2 [179,180], Al_2O_3 [181], and ZnO:Al (AZO) [182,183], has been attempted and the films exhibit improved thermochromic properties. In addition, artificial nanostructures, such as multilayers, porous structures and composites, have also been constructed to compensate the shortcomings of VO_2 thin films alone and to add anti-reflection, anti-fogging, and other functions [184–186]. Fig. 18(c) summarizes the thermochromic performance of different structures based on VO_2 thin films, where it can be seen that porous, multi-layer, and composite structures outperform the VO_2 thin film alone [5]. Fig. 18(d) shows that with a W-doped VO_2 window coating, the internal temperature of a model house is significantly lower (by ∼9 °C) than the one without W-doped VO_2 coating under similar condition of infrared radiation. Further developments of both high-quality materials and optimized structures would be needed to advance VO_2 toward commercial thermochromic materials.

Transistor and electrostatically driven switch

Field-effect transistor (FET) is a three-terminal device that consists of a semiconductor channel to conduct electricity and a capacitor (gate) to tune the carrier density of the channel by electrostatic charging effect. Although metal–oxide-semiconductor FET (MOSFET) has become the fundamental building block of modern electronics, the short channel effect and the current leakage increasingly hinder its further miniaturization. Therefore, a lot of research interests exist in developing novel types of FETs based on other mechanisms.

Strongly correlated materials could be utilized as the channel in an FET but operating on a quite different mechanism, namely, a "Mott transistor" [187]. The Mott transistor works by electrostatically screening the Coulomb interactions in a Mott insulator (OFF state), hence collapsing the bandgap and liberating electrons in the lower Hubbard band, resulting in a metallically conductive channel (ON state) [93]. The Mott transistor would have advantages over MOSFET such as elimination of the dopant fluctuation effect that becomes serious with downscaling of MOSFETs, intrinsically higher switching speed, and potentially sharper subthreshold swing. Although it is still in debate whether the MIT in VO_2 can be classified as a Mott transition, VO_2 has nevertheless been explored as the channel material in the concept of Mott transistors [4,188–190].

However, unlike in a MOSFET where the channel conductivity varies continuously with the gate field, in a Mott insulator the field needs to exceed a threshold value to screen the electron interactions and drive the material into the metallic state. The threshold free carrier density for triggering the MIT of VO_2 (10^{18}–10^{19}/cm^3) is too high to be achieved by conventional solid gating [192,193]. Therefore, liquid gating that uses electrolyte or ionic liquid has been adopted by several groups to construct VO_2 FETs (Fig. 19(a)) [93,95,191,194–196]. Liquid gating achieves a high density of charge accumulation in VO_2 but obviously at the cost of risking chemical reactions and sacrificing its intrinsically fast MIT speed, because ionic motion is involved in the gating process. Experimental results show one to three orders of magnitude change in electrical resistance of the VO_2 channel over a small range of gate voltage (∼3 V) but with a wide hysteresis (Fig. 19(b)). However, the underlying mechanism of this gated MIT has been explained in different ways. Nakano et al. observed
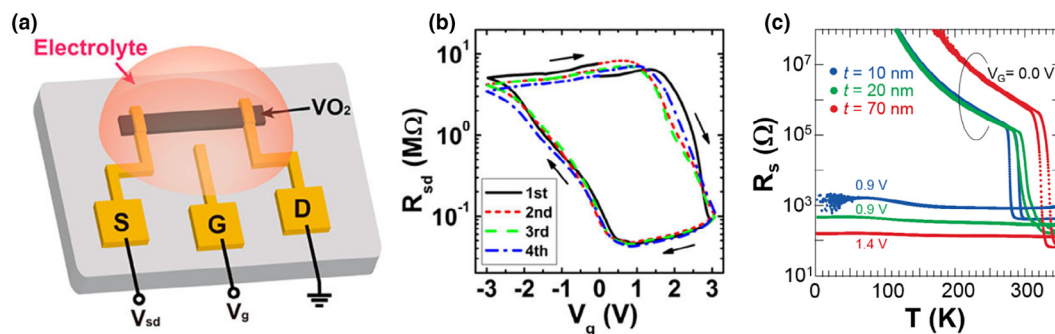

FIGURE 19

(a) Schematic of a liquid-gated FET configuration based on single-crystal VO_2 nanobeam [191]. (b) Source-drain resistance of a VO_2 nanobeam as a function of gate voltage for several scans [191]. (c) Temperature dependence of sheet resistance for VO_2 thin films with different thicknesses at two gate voltages, showing E-field-induced metallic states [93].

a structural phase transition by gating, and attributed the gating effect to bulk carrier delocalization across the MIT triggered by the electrostatic field (Fig. 19(c)) [93]. Liu et al. also concluded the electrostatic gating effect but claimed the existence of a surface MIT of the VO₂ channel because the induced surface metallic layer would strongly screen the gating electric field and prevent further metallization of the VO₂ at a greater depth [191]. However, as a wide hysteresis exists in the transconduction curves, which is usually a clue of electrochemical activity, the gating mechanism was also attributed to electrochemically driven doping of hydrogen ions [195] or oxygen vacancies [95]. Zhou et al. reported a controlled gating experiment of VO₂ films coated with a monolayer graphene as a diffusion barrier for ions, in which they observed suppression of the resistance modulation [196]. It should be cautioned, in analyzing experimental evidence of gate-field activated MIT in VO₂, that Joule heating from leakage current or Poole–Frenkel emission [197], rather than electrostatic charge injection, must be first ruled out. These controversies on the fundamental mechanism, as well as the high threshold for switching, indicate that VO₂-based transistors have a long way to go before they can be considered for practical applications.

Micro-actuation and micro solid engine

Owing to the high elastic modulus for both M1 and R phase (~140 GPa), the large transformation strain across the MIT of VO₂ could be used to drive motion with large forces, promising an effective way to construct a microscale "solid engine". The energy merit of such transformation strain driven actuation is given by the work density, $1/2\, E \cdot \varepsilon^2$, where E is the elastic modulus and ε is the strain. The work density describes the volumetric work output of the working material [198]. Currently, various transducing materials or structures are used to transduce a wide range of stimulating energies into mechanical motion. However, there comes a limit for the materials in delivering both large actuation amplitude (determined by ε) and high force (determined by E). For example, human muscles can extend or shrink along certain direction by over tens of percent but its modulus is quite low (<1 MPa), which results in a work density of only ~0.08 J/cm³. In contrast, the piezoelectric material lead zirconium titanate (PZT) has a large elastic modulus but its strain is low, usually ~0.1% under a voltage of hundreds of volts, also resulting in a low work density of only 0.01–0.1 J/cm³. Fig. 20(a) shows that most conventional actuation materials including piezoelectric materials, electro-simulated polymers, and magnetostrictive materials all have relatively low work densities of <1 J/cm³. VO₂ is a new, promising material in this application, as the work density of its single-crystal reaches up to 10 J/cm³. This value is comparable to that of shape memory alloys (SMA), but SMAs typically have short cyclic lifetimes and are intrinsically difficult to process at the micro-nano scales limited by their domain sizes. The energy efficiency of the actuation with VO₂ is also high. Theoretical analysis estimates the energy efficiency of the heat-to-mechanical energy conversion with VO₂ reaches up to ~8%, which is close to the thermodynamic efficiency limit (Carnot engine under similar conditions, ~12%, Fig. 20(b,c)) [199].
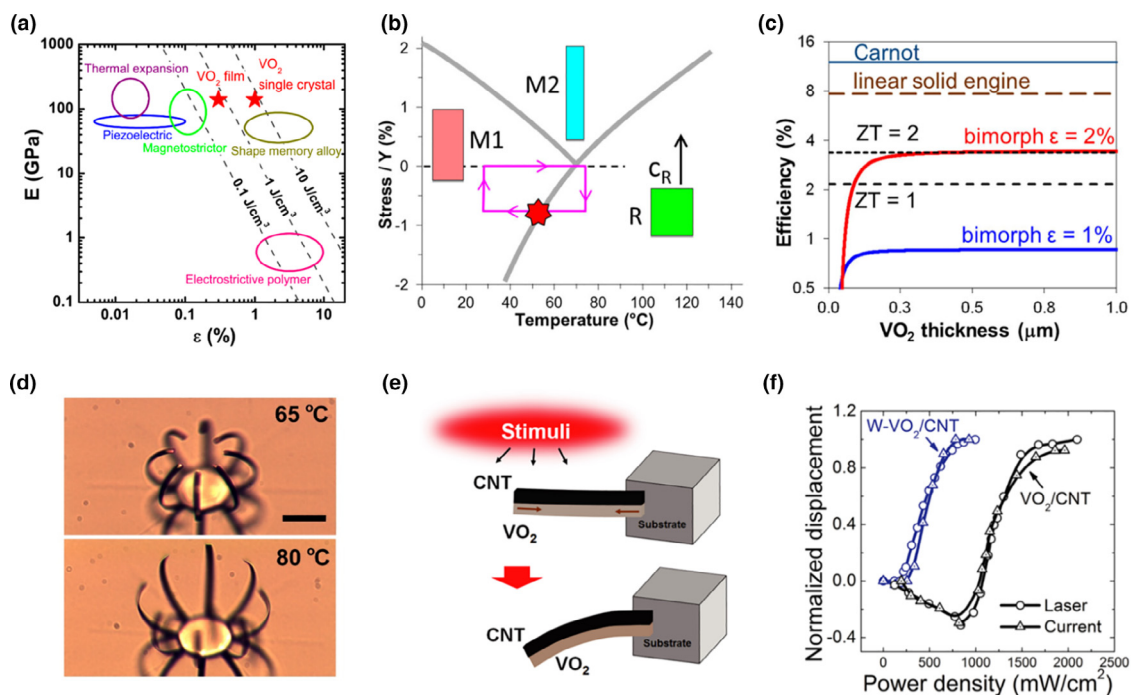

FIGURE 20

(a) Comparison of work densities of various actuation materials [205]. (b) Phase diagram (c_R stress vs temperature) of VO₂. The rectangular loop shows a possible cycle of the solid engine, and the red star is the point where the work is done [199]. The rectangular boxes show schematically the size and shape of the single crystal in the three phases, respectively. (c) Calculated energy efficiency of a VO₂-based linear solid engine and bimorph solid engines for transformation strain of $\varepsilon = 1\%$ (M1-R) and 2% (M2-R) [199]. (d) Microactuator with a "palm" structure, showing the fingers closed at 65 °C and open at 80 °C. Scale bar, 50 μm [205]. (e) Schematic of a flexible VO₂/CNT bilayer actuator [206]. (f) Comparison of the performance of bilayer actuators based on W-doped and undoped VO₂ thin films under light illumination [206].
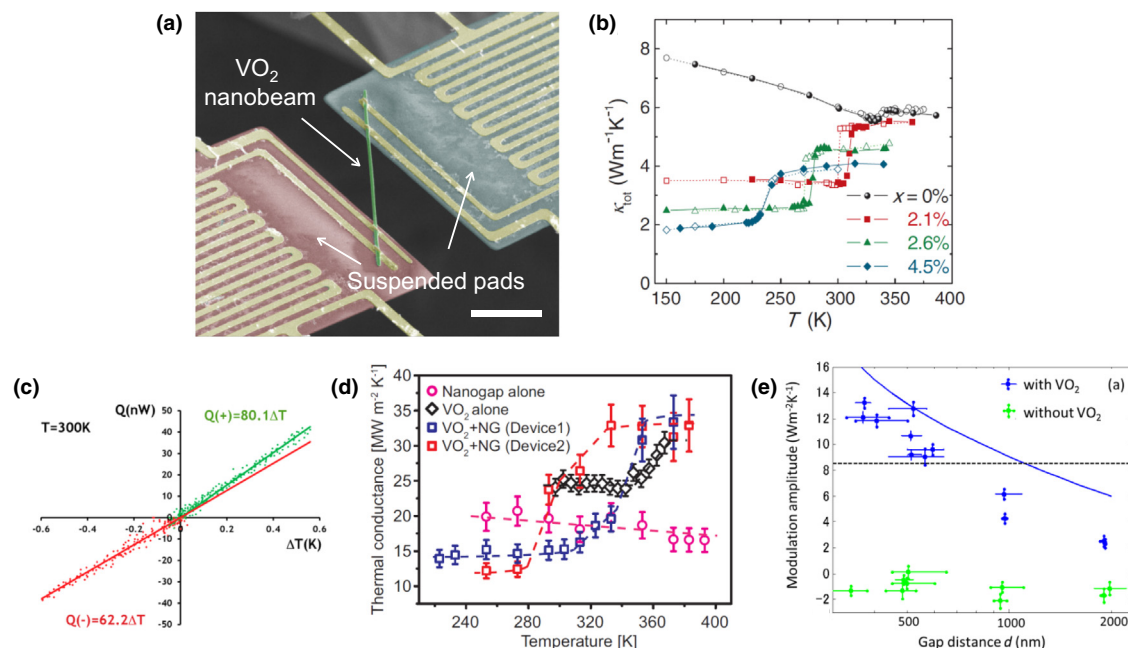
FIGURE 21

(a) SEM image of a suspended-microdevice, for thermal conductivity measurements, consisting of two T-sensing pads (red for high T and blue for low T) and a VO$_2$ nanobeam (green) [54]. Scale bar, 10 μm. (b) Experimentally measured total thermal conductivity of W$_x$V$_{1-x}$O$_2$ nanowires [54]. (c) Heat flow (Q) as a function of ΔT across a tapered VO$_2$ nanowire at 300 K. Different signs (+) and (−) of Q represent different directions of heat transfer. Thermal conductance, i.e. the slope Q/ΔT, differs depending on the direction of the heat flow [218]. (d) Temperature dependence of cross-plane thermal conductance of solid-state nanomechanical thin-film structures having nanogap (NG) alone, VO$_2$ film alone, and VO$_2$ plus NG (Device1 and Device2) [217]. (e) Modulation amplitudes (defined as the value of heat transfer coefficient at 295 K (M1) minus that at 325 K (R)) measured by radiative heat transfer through the nanogap between a SiO$_2$ emitter and W$_x$V$_{1-x}$O$_2$/SiO$_2$ receiver [219].

Mechanical actuation can be experimentally observed in suspended single-crystalline VO$_2$ nanoplatelets [200], or suspended VO$_2$ thin films [201]. These modes of actuation, however, deliver very small amplitudes of actuation. Instead, heterogeneous designs, such as a bilayer structure (bimorph), were employed as they could convert the longitudinal strain of VO$_2$ into a much amplified bending motion of the bilayer. The design of first VO$_2$-based bilayer actuators consisted of VO$_2$-coated Si cantilevers [202]. A Cr-coated VO$_2$ nanowire structure was subsequently developed with a giant bending amplitude, where Cr was selected because of its high modulus and good wettability with VO$_2$ [203]. The initial state of the bilayer actuators is usually curved because of built-in interface stress during the deposition of films, while a flat initial curvature is desired for many applications. Such initial curvature can be compensated using a "seesaw"-type tri-layer design [204]. The other issue is that across the narrow temperature window of MIT, the actuated motion is usually abrupt and difficult to control. This can be alleviated by a gradient doping of the VO$_2$ that expands the temperature window of the MIT [166].

With the bilayer design, the VO$_2$-based bilayer actuators have been used in micro-electro-mechanical systems (MEMS) as cantilevers and mirrors [207–209]. Besides thermal and electro-thermal actuation, photo-thermal actuation also attracts attention because it provides a remote and wireless way of control. Carbon nanotubes (CNTs) were incorporated into the bilayer actuators to improve their light absorption for more efficient photo-thermal actuation [210,211]. Going beyond the

nanowire/nanoplatelets-based bilayer cantilevers, Liu et al. developed microfabrication steps to pattern micro-scale Cr/VO$_2$ thin film actuators into a diverse range of shapes and structures (Fig. 20(d)) [205,212]. These functional structures could be used to catch or release tiny objects, work in ambient or aqueous environment, and more importantly, be triggered by diverse types of stimuli ranging from direct heat, electric current, to light illumination. The bending amplitude is high and the actuation frequency reaches up to ∼6 kHz [205]. Further fashioned into coils, the Cr/VO$_2$ thin film actuators can deliver torsional motion, at speeds as fast as 200,000 rpm and a peak power density of ∼39 kW/kg, operating without material fatigue even after one million cycles of actuation [212]. Such microscopic bending and torsional machines could become the key building blocks in robotics, artificial muscles, smart shutters, and biochemical drug delivery. Flexible actuators were also realized by depositing VO$_2$ on nano-materials such as carbon nanotubes (CNTs) (Fig. 20(e)) [206]. Using the W-doped technique to lower the MIT temperature of VO$_2$, these VO$_2$/CNT flexible actuators can be triggered by sun light illumination or by human-body temperature (Fig. 20(f)).

Regulation of thermal energy

Thermal conductivity of VO$_2$ has been reported several times but with inconsistencies. In the case of bulk samples, the thermal conductivity was reported to be almost constant [40] or decrease very slightly across the MIT [213]. On the other hand, polycrystalline thin film showed a total thermal conductivity in

the metal phase of VO_2 increased from the insulator phase by an amount as much as the value expected by the Wiedemann–Franz (WF) law ($\kappa_e/\sigma = LT$, where κ_e is the electronic thermal conductivity, σ the electrical conductivity, and L the Lorenz number, equal to $L_0 = 2.44 \times 10^{-8}$ WΩ/K^2) [214]. In this case, the VO_2 thin film behaves effectively as a thermal switch, as it drastically changes the total thermal conductivity over a narrow temperature range. Recently, total, electronic, and lattice thermal conductivities of VO_2 were reported, by measuring single crystalline VO_2 nanowires using a suspended microdevice system (Fig. 21(a)) [54]. Using this method, the extrinsic domain and strain effects are minimized, and both electricity and heat flow along the same direction (c_R direction) along the nanowire. The total thermal conductivity of VO_2 was found to be almost a constant, ~6 W/mK across the MIT. Aided by inelastic X-ray scattering and first principles calculations, the electronic contribution to the thermal conductivity was determined to be 10 times lower than the value expected from the WF law [54]. Another significant, potentially useful result of this study is that the effective Lorenz number of VO_2 recovers toward L_0 with increasing W doping. The total thermal conductivity of the W-doped VO_2 hence shows an abrupt increase across the MIT, as shown in Fig. 21(b), suggesting a way of switching thermal conduction using $W_xV_{1-x}O_2$. Similar effect was recently reported in Cu- doped VO_2 thin films [215]. Therefore, doped-VO_2 is potentially able to regulate heat flow in a way akin to transistors do to electrical current.

In addition, thermal devices rectifying or switching heat flow have been investigated using VO_2 [216–218]. Asymmetric heat conduction in tapered VO_2 nanowires was reported (Fig. 21(c)) [218]. The thermal conductance in this device is lower when heat flows toward the thicker side of the tapered nanowire, corresponding to a record-high thermal rectification of ~28%. A strongly temperature-dependent thermal conduction was recently demonstrated across a VO_2-contained thin film structure [217]. The thermal conduction ON/OFF ratio, as high as ~2.75 (Fig. 21(d)), was achieved by the modulation of an interlayer nanogap in the device driven by the VO_2 structural phase transition. An active modulation of radiative heat transfer using VO_2 thin films was also reported very recently [219]. A large-amplitude modulation of the radiation (Fig. 21(e)) beyond the blackbody limit across the nanogap between a SiO_2 emitter and a SiO_2 receiver was observed when W-doped VO_2 was coated on the receiver.

Metamaterials and other applications

There are several other new areas of applications for VO_2 thin films and nanowires. One is in metamaterials. Metamaterials deliver functions by specific design of microstructures rather than their chemical composition (as with normal materials). They are made from assemblies of single or multiple elements arranged in periodic patterns, and can modulate electromagnetic radiation, heat, or sound in manners not possible in natural materials. Interestingly, a VO_2 thin film could be viewed as a natural, disordered metamaterial when it contains multiple metal and insulator domains in the middle of the MIT. Kats et al. found that VO_2 has a large negative differential thermal emittance across the MIT, meaning that its thermal radiation decreases upon heating [220]. Integrated with a gold metamaterial absorber, a VO_2/Au hybrid meta device achieves electrically triggered control in the mid-infrared region [221]. By exploiting the hysteresis in the MIT, VO_2 thin films have been recently employed by Dong et al. as an all-solid, rewritable metamaterial, coined as a "metacanvas" [222], as shown in Fig. 22. Setting the temperature of the VO_2 to the middle of the hysteresis, arbitrary photonic patterns can be rapidly and repeatedly written on the VO_2 film by a low-power laser and erased by global cooling. Using the metacanvas, dynamic manipulation of optical waves for light propagation, polarization, and reconstruction was demonstrated. It thus offers a route to building photonic elements that can be field programmed to deliver complex, system-level functionalities.

The sensitivity of the MIT with strain, as shown in Fig. 7, has been exploited to make stress sensors, as external stress could drive the MIT and drastically alter the conductance of the system [77,223]. The MIT feature of VO_2 nanowires at a sharp temperature point has enabled applications as microthermometers for quantitative evaluation of electron beam heating, light absorption and heat transfer of other micro-objects [224,225]. The negative differential thermal emittance of VO_2 also finds potential applications in infrared camouflage. Xiao et al. developed an infrared camouflage device based on a layer of VO_2 supported by a graphene-CNT film [226]. A slight joule heating could drastically change the emissivity of the device, achieving a rapidly
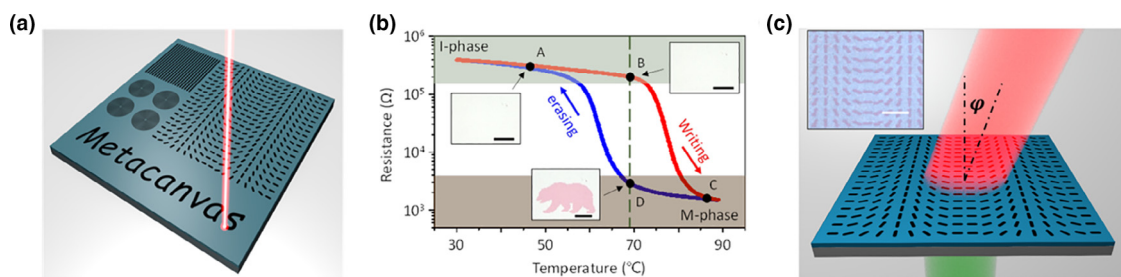

FIGURE 22

(a) Schematic of laser writing different photonic patterns on a meta-canvas [222]. (b) Temperature-dependent resistance of a VO_2 film, where the transition temperature (T_c) is denoted by a vertical dashed line. Inset A and B: un-patterned VO_2 film (all in I-phase). Inset D: the VO_2 film (global temperature kept at T_c) is laser-written with a pattern of a bear in the M-phase [222]. (c) Schematic of a meta-canvas programmed as a beam steerer with a steering angle φ. Inset: optical image of the beam steering phase array compiled on the VO_2 metacanvas (Scale bar is 10 μm in Inset) [222].

responsive (~40 ms), switchable, and low-power consuming infrared camouflage. In the field of energy storage, Yoon et al. reported hydrogen storage application with VO_2 thin films [227]. As many as two hydrogen atoms can be reversibly absorbed into, and released from, each VO_2 unit cell, without destroying its lattice framework. As VO_2 changes its resistivity, optical constants, and lattice structures across its MIT, it has been adopted as an "active" substrate to modulate optical and electronic properties of overlaid two-dimensional materials, such as MoS_2 [228–230]. With these intriguing properties, there is no doubt that VO_2 as a functional material may find more interesting applications in the future.

Summary and perspectives

In this review, we attempt to summarize recent progresses on the physics and applications of VO_2. VO_2 distinguishes itself from other phase change materials with its intrinsically coupled electronic and structural phase transition at a temperature that is conveniently accessible. The phase transition could be readily modulated by non-thermal means including stress, pressure, defects, and electrical fields. Some novel ways to drive the transition have delivered interesting results but in the meantime added fuel to the long-lasting debate on the mechanism of the MIT.

Despite recent progresses, the exact mechanism of the MIT still remains to be fully elucidated. As the MIT in VO_2 is nearly always accompanied by the SPT, a purely Mott or Peierls picture is insufficient to describe the origin of the phase transition. Recent efforts have been made to bridge the gap between these two proposed mechanisms. Investigations of the MIT in response to ultra-fast optical fields, electrostatic fields, THz pulses or stress shed light into the mechanism in an unprecedented way; nevertheless, the dispute will surely continue and develop in the near future.

Advances in more precise control of stoichiometry in growth of thin films and nanostructures have enabled VO_2 to be considered for a wide range of applications, particularly in "smart" devices, where the functions are defined by optical or infrared transmittance/emissivity, electrical conductivity, mechanical motion, or heat flow responding to versatile external stimuli. In the foreseeable future, VO_2 is expected to be still a popular material for research in such "smart" applications.

Currently, high-quality crystalline VO_2 thin films are epitaxially grown on a limited number of substrates (e.g., sapphire and TiO_2). It is much desired to develop recipes to selectively etch these substrates against VO_2, to find new substrates that are functional (e.g., conductive) but in the meantime lattice matched to VO_2, to allow control of domain structure and minimization of micro-cracks and grain boundaries in the VO_2 epi-layer, and to develop deposition methods that are compatible to existing industry standards. In terms of nanostructure growth, it still remains challenging to synthesize free-standing, single-crystalline VO_2 structures over large area and with precise placement on substrates, with ultra-thin thicknesses (<50 nm), controlled shape and size, arbitrary crystal orientation, and desired doping or stoichiometry. Tackling these challenges is particularly important because free-standing VO_2 nanostructures provide advantages over clamped thin films for both exploration of the intrinsic MIT physics and strain-sensitive applications.

Acknowledgments

References

[1] F.J. Morin, Phys. Rev. Lett. 3 (1959) 34.
[2] V. Eyert, Ann. Phys. (Leipzig) 11 (2002) 650.
[3] J. Nag, R.F. Haglund, J. Phys.: Condens. Matter. 20 (2008) 264016.
[4] Z. Yang, C.Y. Ko, S. Ramanathan, Oxide electronics utilizing ultrafast metal-insulator transitions, in: D.R. Clarke, P. Fratzl (Eds.), Annual Review of Materials Research, Annual Reviews, Palo Alto, 2011, pp. 337–367.
[5] Y.F. Gao et al., Nano Energy 1 (2012) 221.
[6] S.F. Wang et al., Prog. Mater. Sci. 81 (2016) 1.
[7] D.B. McWhan et al., Phys. Rev. B 10 (1974) 490.
[8] J.D. Budai et al., Acta Mater. 61 (2013) 2751.
[9] J.B. Goodenough, J. Solid State Chem. 3 (1971) 490.
[10] J.M. Longo, P. Kierkegaard, Acta Chem. Scand. 24 (1970) 420.
[11] R. Heckingbottom, J.W. Linnett, Nature 194 (1962) 678.
[12] M. Marezio et al., Phys. Rev. B 5 (1972) 2541.
[13] G. Villeneuve, M. Drillon, P. Hagenmuller, Mater. Res. Bull. 8 (1973) 1111.
[14] J.P. Pouget et al., Phys. Rev. B 10 (1974) 1801.
[15] A. Tselev et al., Nano Lett. 10 (2010) 4409.
[16] J.H. Park et al., Nature 500 (2013) 431.
[17] J.P. Pouget et al., Phys. Rev. Lett. 35 (1975) 873.
[18] M. Marezio, P. Dernier, A. Santoro, Acta Crystallogr. Sect. A 29 (1973) 618.
[19] X.G. Tan et al., Sci. Rep. 2 (2012) 466.
[20] M. Ghedira et al., J. Solid State Chem. 22 (1977) 423.
[21] W. Fan et al., Phys. Rev. B 83 (2011) 235102.
[22] X. Yuan et al., Phys. Rev. B 86 (2012) 235103.
[23] V. Eyert, Ann. Phys. 11 (2002) 650.
[24] N.B. Aetukuri et al., Nat. Phys. 9 (2013) 661.
[25] A. Zylbersztejn, N.F. Mott, Phys. Rev. B 11 (1975) 4383.
[26] N.F. Mott, L. Friedman, Phil. Mag. 30 (1974) 389.
[27] J.M. Tomczak, F. Aryasetiawan, S. Biermann, Phys. Rev. B 78 (2008) 115103.
[28] R.M. Wentzcovitch, W.W. Schulz, P.B. Allen, Phys. Rev. Lett. 72 (1994) 3389.
[29] V. Eyert, Phys. Rev. Lett. 107 (2011) 016401.
[30] J.D. Budai et al., Nature 515 (2014) 535.
[31] R. Grau-Crespo, H. Wang, U. Schwingenschlögl, Phys. Rev. B 86 (2012) 081101.
[32] S. Biermann et al., Phys. Rev. Lett. 94 (2005) 026404.
[33] H. Zheng, L.K. Wagner, Phys. Rev. Lett. 114 (2015) 176401.
[34] W.H. Brito et al., Phys. Rev. Lett. 117 (2016) 056402.
[35] S. Shin et al., Phys. Rev. B 41 (1990) 4993.
[36] M. Abbate et al., Phys. Rev. B 43 (1991) 7263.
[37] T.C. Koethe et al., Phys. Rev. Lett. 97 (2006) 116402.
[38] A.X. Gray et al., Phys. Rev. Lett. 116 (2016) 116403.
[39] T. Yao et al., Phys. Rev. Lett. 105 (2010) 226405.
[40] C.N. Berglund, H.J. Guggenheim, Phys. Rev. 185 (1969) 1022.
[41] K. Kosuge, J. Phys. Soc. Jpn. 22 (1967) 551.
[42] T. Kawakubo, T. Nakagawa, J. Phys. Soc. Jpn. 19 (1964) 517.
[43] S. Xu et al., Phys. Rev. B 95 (2017) 125105.
[44] B. Lazarovits et al., Phys. Rev. B 81 (2010) 115117.
[45] C. Weber et al., Phys. Rev. Lett. 108 (2012) 256402.
[46] C. Hearn, J. Phys. C: Solid State Phys. 5 (1972) 1317.
[47] F. Gervais, W. Kress, Phys. Rev. B 31 (1985) 4809.

[48] M. Gupta, A.J. Freeman, D.E. Ellis, Phys. Rev. B 16 (1977) 3338.
[49] H. Terauchi, J.B. Cohen, Phys. Rev. B 17 (1978) 2494.
[50] M.M. Qazilbash et al., Science 318 (2007) 1750.
[51] M. Qazilbash et al., Phys. Rev. B 74 (2006) 205118.
[52] J. Zaanen, Nature 430 (2004) 512.
[53] J.A.N. Bruin et al., Science 339 (2013) 804.
[54] S. Lee et al., Science 355 (2017) 371.
[55] V.R. Morrison et al., Science 346 (2014) 445.
[56] J. Cao et al., Phys. Rev. B 82 (2010) 241101.
[57] J. Wei et al., Nat. Nanotechnol. 4 (2009) 420.
[58] M.W. Haverkort et al., Phys. Rev. Lett. 95 (2005) 196404.
[59] R. Srivastava, L.L. Chase, Phys. Rev. Lett. 27 (1971) 727.
[60] P. Schilbe, Physica B 316 (2002) 600.
[61] D. Maurer et al., Phys. Rev. B 60 (1999) 13249.
[62] S. Wall et al., Nat. Commun. 3 (2012) 721.
[63] W. Paul, Mater. Res. Bull. 5 (1970) 691.
[64] S. Kim et al., Phys. Rev. B 87 (2013) 195106.
[65] A. Cavalleri et al., Phys. Rev. Lett. 87 (2001) 237401.
[66] A. Cavalleri et al., Phys. Rev. B 70 (2004) 161102.
[67] P. Baum, D.-S. Yang, A.H. Zewail, Science 318 (2007) 788.
[68] H.T. Kim et al., Phys. Rev. Lett. 97 (2006) 266401.
[69] Z. Tao et al., Sci. Rep. 6 (2016) 38514.
[70] M.F. Becker et al., Appl. Phys. Lett. 65 (1994) 1507.
[71] D. Wegkamp et al., Phys. Rev. Lett. 113 (2014) 216401.
[72] C. Kübler et al., Phys. Rev. Lett. 99 (2007) 116401.
[73] J. Laverock et al., Phys. Rev. Lett. 113 (2014) 216402.
[74] Z. Tao et al., Phys. Rev. Lett. 109 (2012) 166406.
[75] H. Liu et al., J. Electron. Mater. 33 (2004) 1171.
[76] J.Q. Wu et al., Nano Lett. 6 (2006) 2313.
[77] J. Cao et al., Nat. Nanotechnol. 4 (2009) 732.
[78] A. Tselev et al., Nano Lett. 10 (2010) 2003.
[79] J.I. Sohn et al., Nano Lett. 9 (2009) 3392.
[80] S.X. Zhang, J.Y. Chou, L.J. Lauhon, Nano Lett. 9 (2009) 4527.
[81] J.M. Booth, P.S. Casey, ACS Appl. Mater. Interfaces 1 (2009) 1899.
[82] A.C. Jones et al., Nano Lett. 10 (2010) 1574.
[83] J. Cao et al., Nano Lett. 10 (2010) 2667.
[84] D. Kucharczyk, T. Niklewski, J. Appl. Crystallogr. 12 (1979) 370.
[85] O.A. Cook, J. Am. Chem. Soc. 69 (1947) 331.
[86] C.N. Berglund, A. Jayaraman, Phys. Rev. 185 (1969) 1034.
[87] T.M. Rice, H. Launois, J.P. Pouget, Phys. Rev. Lett. 73 (1994) 3042.
[88] J.M. Atkin et al., Phys. Rev. B 85 (2012) 020101.
[89] L.G. Bai et al., Phys. Rev. B 91 (2015) 104110.
[90] C. Marini et al., High Pressure Res. 30 (2010) 55.
[91] Y.B. Chen et al., Nano Lett. 17 (2017) 2512.
[92] N.F. Quackenbush et al., Phys. Rev. B 94 (2016). 085105.
[93] M. Nakano et al., Nature 487 (2012) 459.
[94] Y.J. Cui, S. Ramanathan, J. Vac. Sci. Technol. A 29 (2011). 041502.
[95] J. Jeong et al., Science 339 (2013) 1402.
[96] W. Brückner et al., Phys. Status Solidi A-Appl. Res. 29 (1975) 63.
[97] N. Kimizuka et al., J. Solid State Chem. 9 (1974) 69.
[98] J. Wei et al., Nat. Nanotechnol. 7 (2012) 357.
[99] S.X. Zhang, I.S. Kim, L.J. Lauhon, Nano Lett. 11 (2011) 1443.
[100] Z. Zhang et al., Phys. Rev. Appl. 7 (2017). 034008.
[101] C.H. Griffiths, H.K. Eastwood, J. Appl. Phys. 45 (1974) 2201.
[102] K. Kosuge, J. Phys. Chem. Solids 28 (1967) 1613.
[103] Y.B. Kang, J. Eur. Ceram. Soc. 32 (2012) 3187.
[104] N. Bahlawane, D. Lenoble, Chem. Vapor Depos. 20 (2014) 299.
[105] U. Schwingenschlögl, V. Eyert, Ann. Phys. (Leipzig) 13 (2004) 475.
[106] S. Kachi, K. Kosuge, H. Okinaka, J. Solid State Chem. 6 (1973) 258.
[107] D.B. McWhan et al., Phys. Rev. B 7 (1973) 1920.
[108] B. Fisher, J. Genossar, G.M. Reisner, Solid State Commun. 226 (2016) 29.
[109] T. Toriyama et al., Phys. Rev. B 90 (2014). 085131.
[110] D.Y. Fu et al., J. Appl. Phys. 113 (2013). 043707.
[111] H. Karl, J. Dreher, B. Stritzker, Semiconductor-metal phase transition in doped ion beam synthesized VO(2) nanoclusters, in: J. Wu, W.Q. Han, A. Janotti, H. C. Kim (Eds.), Functional Metal-Oxide Nanostructures, Materials Research Society, Warrendale, 2009, pp. 107–112.
[112] H. Hofsass et al., AIP Adv. 1 (2011). 032168.
[113] J.G. Ramirez et al., Phys. Rev. B 91 (2015) 205123.
[114] J.B. MacChesney, J. Phys. Chem. Solids 30 (1969) 225.
[115] M. Nygren, M. Israelsson, Mater. Res. Bull. 4 (1969) 881.
[116] B.L. Chamberland, Mater. Res. Bull. 6 (1971) 425.
[117] G. Villeneuve et al., Mater. Res. Bull. 6 (1971) 119.

[118] T. Hörlin, Mater. Res. Bull. 7 (1972) 1515.
[119] M. Drillon, G. Villeneuve, Mater. Res. Bull. 9 (1974) 1199.
[120] T. Hörlin, T. Niklewski, M. Nygren, Acta Chem. Scand. A 30 (1976) 619.
[121] K. Kosuge, S. Kachi, Mater. Res. Bull. 11 (1976) 255.
[122] G. Villeneuve et al., J. Phys. C Solid State Phys. 10 (1977) 3621.
[123] F. Pintchovski, W.S. Glausinger, A. Navrotsky, J. Phys. Chem. Solids 39 (1978) 941.
[124] W. Brückner et al., J. Phys. Colloques 37 (1976) C4–C63.
[125] T. Hörlin, T. Niklewski, M. Nygren, J. Phys. Colloques 37 (1976) C4–C69.
[126] J.P. Pouget, H. Launois, J. Phys. Colloques 37 (1976) C4–49.
[127] N. Wang et al., J. Mater. Chem. C 3 (2015) 6771.
[128] K. Miyazaki et al., Jpn. J. Appl. Phys. 53 (2014). 071102.
[129] M. Nishikawa et al., Jpn. J. Appl. Phys. 50 (2011). 01be04.
[130] J.C. Rakotoniaina et al., J. Solid State Chem. 103 (1993) 81.
[131] P. Jin et al., Thin Solid Films 375 (2000) 128.
[132] Q. Gu et al., Nano Lett. 7 (2007) 363.
[133] O.Y. Berezina et al., Inorg. Mater. 43 (2007) 505.
[134] N.R. Mlyuka, G.A. Niklasson, C.G. Granqvist, Appl. Phys. Lett. 95 (2009) 171909.
[135] A. Krammer et al., J. Appl. Phys. 122 (2017). 045304.
[136] S.J. Liu et al., Jpn. J. Appl. Phys. 53 (2014). 063201.
[137] E. Strelcov et al., Nano Lett. 12 (2012) 6198.
[138] N. Wang et al., J. Alloy. Compd. 711 (2017) 222.
[139] N. Wang et al., RSC Adv. 6 (2016) 48455.
[140] R.L. Remke, R.M. Walser, R.W. Bene, Thin Solid Films 61 (1979) 73.
[141] C.B. Greenberg, Thin Solid Films 110 (1983) 73.
[142] Y. Takahashi et al., J. Mater. Sci. 24 (1989) 192.
[143] T. Maruyama, Y. Ikuta, J. Mater. Sci. 28 (1993) 5073.
[144] T.D. Manning et al., Chem. Mater. 16 (2004) 744.
[145] D.P. Partlow et al., J. Appl. Phys. 70 (1991) 443.
[146] S.W. Lu, L.S. Hou, F.X. Gan, Adv. Mater. 9 (1997) 244.
[147] B.G. Chae et al., Electrochem. Solid State Lett. 9 (2006) C12.
[148] C.C.Y. Kwan, C.H. Griffiths, H.K. Eastwood, Appl. Phys. Lett. 20 (1972) 93.
[149] F. Beteille, L. Mazerolles, J. Livage, Mater. Res. Bull. 34 (1999) 2177.
[150] D. Brassard et al., Appl. Phys. Lett. 87 (2005). 051910.
[151] D.H. Kim, H.S. Kwok, Appl. Phys. Lett. 65 (1994) 3188.
[152] Y.X. Guo et al., Appl. Phys. A-Mater. Sci. Process. 115 (2014) 1245.
[153] R. McGee et al., Acta Mater. 137 (2017) 12.
[154] X. Cao et al., Langmuir 30 (2014) 1710.
[155] Y.M. Li et al., Mater. Interfaces 5 (2013) 6603.
[156] L.Q. Mai et al., J. Phys. Chem. B 110 (2006) 19083.
[157] G.A. Horrocks et al., Mater. Interfaces 6 (2014) 15726.
[158] L. Whittaker, H.S. Zhang, S. Banerjee, J. Mater. Chem. 19 (2009) 2968.
[159] H.H. Yin et al., Physica E 43 (2011) 1720.
[160] L. Whittaker et al., J. Am. Chem. Soc. 131 (2009) 8884.
[161] B.S. Guiton et al., J. Am. Chem. Soc. 127 (2005) 498.
[162] J.M. Baik et al., J. Phys. Chem. C 112 (2008) 13328.
[163] M.H. Kim et al., Nano Lett. 9 (2009) 4138.
[164] Y. Cheng et al., J. Cryst. Growth 311 (2009) 1571.
[165] E. Strelcov et al., ACS Nano 5 (2011) 3373.
[166] S. Lee et al., J. Am. Chem. Soc. 135 (2013) 4850.
[167] C. Cheng et al., Appl. Phys. Lett. 100 (2012) 103111.
[168] H.A. Wriedt, Bull. Alloy Phase Diagr. 10 (1989) 271.
[169] J. Maeng et al., Mater. Res. Bull. 43 (2008) 1649.
[170] J.I. Sohn et al., Nano Lett. 7 (2007) 1570.
[171] J.Y. Chou et al., J. Appl. Phys. 105 (2009) 034310.
[172] C. Cheng et al., Sci. Rep. 4 (2014) 5456.
[173] M. Gurvitch et al., J. Appl. Phys. 106 (2009) 104504.
[174] F. Niklaus, C. Vieider, H. Jakobsen, MEMS-Based uncooled infrared bolometer Arrays – A review, in: J.C. Chiao, X. Chen, Z. Zhou, X. Li (Eds.), MEMS/ MOEMS Technologies and Applications III, Spie-Int Soc Optical Engineering, Bellingham, 2008.
[175] M. Soltani et al., J. Vac. Sci. Technol. A 25 (2007) 971.
[176] H. Takami et al., Jpn. J. Appl. Phys. 50 (2011). 055804.
[177] W. Burkhardt et al., Thin Solid Films 402 (2002) 226.
[178] J.D. Zhou et al., Phys. Chem. Chem. Phys. 15 (2013) 7505.
[179] H. Koo et al., J. Mater. Eng. Perform. 22 (2013) 3967.
[180] Z.T. Zhang et al., J. Phys. Chem. C 114 (2010) 22214.
[181] Y. Xiong et al., J. Phys. D-Appl. Phys. 47 (2014) 455304.
[182] L.T. Kang et al., Sol. Energy Mater. Sol. Cells 95 (2011) 3189.
[183] X.H. Chu et al., J. Non-Cryst. Solids 383 (2014) 121.
[184] C. Liu, N. Wang, Y. Long, Appl. Surf. Sci. 283 (2013) 222.
[185] Z. Chen et al., Sol. Energy Mater. Sol. Cells 95 (2011) 2677.

[186] J.Y. Zheng, S.H. Bao, P. Jin, Nano Energy 11 (2015) 136.
[187] D.M. Newns et al., Appl. Phys. Lett. 73 (1998) 780.
[188] H.T. Kim et al., New J. Phys. 6 (2004) 52.
[189] D. Ruzmetov et al., J. Appl. Phys. 107 (2010) 114516.
[190] Y. Zhou, S. Ramanathan, Proc. IEEE 103 (2015) 1289.
[191] K. Liu et al., Nano Lett. 12 (2012) 6272.
[192] S. Hormoz, S. Ramanathan, Solid-State Electron. 54 (2010) 654.
[193] S. Sengupta et al., Appl. Phys. Lett. 99 (2011). 062114.
[194] Z. Yang, Y. Zhou, S. Ramanathan, J. Appl. Phys. 111 (2012). 014506.
[195] H. Ji, J. Wei, D. Natelson, Nano Lett. 12 (2012) 2988.
[196] Y. Zhou et al., Nano Lett. 15 (2015) 1627.
[197] C. Ko, S. Ramanathan, Appl. Phys. Lett. 93 (2008).
[198] T. Mirfakhrai, J.D.W. Madden, R.H. Baughman, Mater. Today 10 (2007) 30.
[199] K. Wang et al., ACS Nano 7 (2013) 2266.
[200] A. Tselev et al., Nano Lett. 11 (2011) 3065.
[201] N. Manca et al., Adv. Mater. 29 (2017) 1701618.
[202] A. Rua, F.E. Fernandez, N. Sepulveda, J. Appl. Phys. 107 (2010). 074506.
[203] J.B. Cao et al., J. Appl. Phys. 108 (2010). 083538.
[204] K.C. Dong et al., Appl. Phys. Lett. 109 (2016). 023504.
[205] K. Liu et al., Nano Lett. 12 (2012) 6302.
[206] H. Ma et al., Nano Lett. 17 (2017) 421.
[207] R. Cabrera, E. Merced, N. Sepulveda, J. Microelectromech. Syst. 23 (2014) 243.
[208] D. Torres et al., J. Microelectromech. Syst. 25 (2016) 780.

[209] B. Viswanath, S. Ramanathan, Nanoscale 5 (2013) 7484.
[210] T.Y. Wang et al., ACS Nano 9 (2015) 4371.
[211] T. Wang et al., Sci. Adv. 3 (2017) 1602697.
[212] K. Liu et al., Adv. Mater. 26 (2014) 1746.
[213] V.N. Andreev et al., Phys. Status Solidi A-Appl. Res. 48 (1978) K153.
[214] D.W. Oh et al., Appl. Phys. Lett. 96 (2010) 151906.
[215] K. Dahal et al., J. Appl. Phys. 121 (2017) 155103.
[216] Y. Zhou et al., IEEE Electron Device Lett. 34 (2013) 220.
[217] H.S. Choe et al., Sci. Rep. 7 (2017) 7131.
[218] J. Zhu et al., Nano Lett. 14 (2014) 4867.
[219] K. Ito et al., Nano Lett. 17 (2017) 4347.
[220] M.A. Kats et al., Phys. Rev. X 3 (2013). 041004.
[221] L. Liu et al., Nat. Commun. 7 (2016) 13236.
[222] K. Dong et al., Adv. Mater. 30 (2018) 1703878.
[223] B. Hu et al., Adv. Mater. 22 (2010) 5134.
[224] H. Guo et al., Nat. Commun. 5 (2014) 4986.
[225] C. Cheng et al., Adv. Opt. Mater. 3 (2015) 336.
[226] L. Xiao et al., Nano Lett. 15 (2015) 8365.
[227] H. Yoon et al., Nat. Mater. 15 (2016) 1113.
[228] J.W. Hou et al., Small 12 (2016) 3976.
[229] Y.C. Lin et al., J. Phys.-Cond. Matter 28 (2016) 504001.
[230] Y.H. Sun, R.M. Wang, K. Liu, Appl. Phys. Rev. 4 (2017). 011301.